



A Population of Luminous Globular Clusters and Stripped Nuclei with Elevated Mass to Light Ratios around NGC 5128*

Antoine Dumont¹, Anil C. Seth¹, Jay Strader², Karina Voggel³, David J. Sand⁴, Allison K. Hughes⁴,
Nelson Caldwell⁵, Denija Crnojević⁶, Mario Mateo², John I. Bailey, III⁷, and Duncan A. Forbes⁸

¹ Department of Physics and Astronomy, University of Utah 115 South 1400 East, Salt Lake City, UT 84112, USA; antoine.dumont.neira@hotmail.com, seth@astro.utah.edu

² Department of Physics and Astronomy Michigan State University Biomedical & Physical Sciences 567 Wilson Rd, Room 3275 East Lansing, MI 48824-2320, USA; strader@pa.msu.edu

³ Université de Strasbourg, CNRS, Observatoire astronomique de Strasbourg, UMR 7550, F-67000 Strasbourg, France

⁴ Steward Observatory, University of Arizona, 933 North Cherry Avenue, Tucson, AZ 85721, USA

⁵ Center for Astrophysics, Harvard & Smithsonian, 60 Garden Street, Cambridge, MA 02138, USA

⁶ University of Tampa, 401 West Kennedy Boulevard, Tampa, FL 33606, USA

⁷ Department of Physics Broida Hall, University of California, Santa Barbara, CA 93106, USA

⁸ Centre for Astrophysics & Supercomputing, Swinburne University, Hawthorn, VIC 3122, Australia

Received 2021 September 30; revised 2022 January 5; accepted 2022 January 19; published 2022 April 21

Abstract

The dense central regions of tidally disrupted galaxies can survive as ultracompact dwarfs (UCDs) that hide among the luminous globular clusters (GCs) in the halo of massive galaxies. An exciting confirmation of this model is the detection of overmassive black holes in the centers of some UCDs, which also lead to elevated dynamical mass-to-light ratios (M/L_{dyn}). Here we present new high-resolution spectroscopic observations of 321 luminous GC candidates in the massive galaxy NGC 5128/Centaurus A. Using these data we confirm 27 new luminous GCs, and measure velocity dispersions for 57 luminous GCs (with g -band luminosities between 2.5×10^5 and $2.5 \times 10^7 L_{\odot}$), of which 48 are new measurements. Combining these data with size measurements from Gaia, we determine the M/L_{dyn} for all 57 luminous GCs. We see a clear bimodality in the M/L_{dyn} distribution, with a population of normal GCs with mean $M/L_{\text{dyn}} = 1.51 \pm 0.31$, and a second population of ~ 20 GCs with elevated mean $M/L_{\text{dyn}} = 2.68 \pm 0.22$. We show that black holes with masses $\sim 4\%$ – 18% of the luminous GCs can explain the elevated mass-to-light ratios. Hence, it is plausible that the NGC 5128 sources with elevated M/L_{dyn} are mostly stripped galaxy nuclei that contain massive central black holes, though future high spatial resolution observations are necessary to confirm this hypothesis for individual sources. We also present a detailed discussion of an extreme outlier, *VHH81-01*, one of the largest and most massive GC in NGC 5128, making it an exceptionally strong candidate to be a tidally stripped nucleus.

Unified Astronomy Thesaurus concepts: Ultracompact dwarf galaxies (1734); Globular star clusters (656); Mass-to-light ratio (1011); Galaxy nuclei (609); Stellar kinematics (1608); Stellar dynamics (1596)

Supporting material: machine-readable tables

1. Introduction

A majority of lower-mass galaxies host dense nuclear star clusters (Neumayer et al. 2020). During merging, the tidal forces of a larger galaxy can strip away the contents of a smaller one, leaving behind these nuclear star clusters to orbit in the halo of the larger galaxy as a stripped galaxy nucleus (e.g., Pfeffer & Baumgardt 2013). Such stripped galaxy nuclei can be challenging to distinguish from massive globular clusters (GCs). The collection of massive GCs and stripped galaxy nuclei is often referred to as ultracompact dwarf galaxies (UCD). The physical definition of UCDs varies widely in the literature (e.g., Mieske et al. 2013; Liu et al. 2015), but commonly refers to objects with $\gtrsim 2 \times 10^6 M_{\odot}$ and half-light radii of $\gtrsim 7$ – 10 pc (e.g., Mieske & Kroupa 2008; Forbes & Kroupa 2011). However, nuclear star clusters extend down to

lower masses and sizes than commonly used cutoffs for defining UCDs and can overlap in mass and size with GCs (Neumayer et al. 2020). Thus the definitions of UCDs neither exclude all massive GCs nor include all stripped nuclei. Because of the ambiguity in the classification of UCDs, throughout this paper we use the term *luminous GCs*. These luminous GCs refer to both massive GCs and stripped galaxy nuclei without assuming a specific mass, luminosity, or size cut.

A large number of stripped nuclei are expected around massive galaxies and in galaxy clusters due to the hierarchical nature of galaxy merging. Simulations are consistent with most of the higher mass GCs ($\gtrsim 10^7 M_{\odot}$) in clusters being stripped galaxy nuclei (Pfeffer et al. 2016; Norris et al. 2019; Mayes et al. 2021). They also suggest that lower-mass galaxies will contain lower-mass stripped nuclei, and that the Milky Way may contain 2–6 stripped nuclei (Pfeffer et al. 2014; Kruijssen et al. 2019).

Stripped nuclei can be distinguished observationally from normal GCs due to their lives at the centers of galaxies; this can result in extended star formation and the growth of massive black holes (e.g., Neumayer et al. 2020). Within the Milky Way, evidence for large metallicity and age spreads is seen in

* This paper includes data gathered with the 6.5 m Magellan Telescope at Las Campanas Observatory, Chile.



Original content from this work may be used under the terms of the [Creative Commons Attribution 4.0 licence](https://creativecommons.org/licenses/by/4.0/). Any further distribution of this work must maintain attribution to the author(s) and the title of the work, journal citation and DOI.

several luminous GCs, including ω Cen (e.g., Johnson & Pilachowski 2010; Villanova et al. 2014), which appears to be the nucleus of a significant building block of the Milky Way (Forbes 2020; Pfeffer et al. 2021), and M54 (Siegel et al. 2007; Alfaro-Cuello et al. 2019), which is the nucleus of the currently infalling Sagittarius dwarf galaxy. An extended star formation history has also been seen in a massive ($3 \times 10^7 M_\odot$) UCD around NGC 4546 (Norris et al. 2015).

It is now well established that supermassive black holes are common at the centers of galaxies with stellar mass $M_\star > 10^9 M_\odot$, including those with nuclear star clusters (Miller et al. 2015; Nguyen et al. 2018, 2019; Greene et al. 2020). Thus we expect stripped nuclei to host massive black holes as well. Supermassive black holes (SMBHs) have been dynamically detected in all five massive UCDs ($>10^7 M_\odot$) with available high spatial resolution integral field spectroscopic data (Seth et al. 2014; Ahn et al. 2017, 2018; Afanasiev et al. 2018). The black holes in these UCDs typically make up $\sim 10\%$ of their total stellar mass, similar to the mass fraction of the SMBH in the nuclear star cluster of the Milky Way (Neumayer et al. 2020). As noted above, simulations suggest that all UCDs in this mass range should be stripped nuclei (Pfeffer et al. 2016; Mayes et al. 2021). These same simulations suggest that many stripped nuclei should have lower masses as well ($<10^7 M_\odot$). The star formation histories of ω Cen and M54 discussed above confirm that there are stripped nuclei at lower masses, as does the recent detection of a $\sim 10^5 M_\odot$ black hole in Andromeda’s most massive GC (Pechetti et al. 2022).

There have also been many claims of detections of $\lesssim 10^4 M_\odot$ black holes at the centers of Milky Way GCs (see recent review by Greene et al. 2020). However, none of these claims is regarded as robust (e.g., Zocchi et al. 2019; Hénault-Brunet et al. 2020), and no accretion evidence for any intermediate mass black holes in Milky Way GCs have been found (Tremou et al. 2018). The claimed detections and upper limits for these black holes correspond to mass fraction of 0.1%–1% of the total mass of the cluster. Theoretically, there are processes that may form intermediate mass black holes during the formation and evolution of GCs, including the merging of massive stars early in the life of the cluster or the merging of stellar mass black holes over time (e.g., Portegies Zwart et al. 2004; Inayoshi et al. 2020; Di Carlo et al. 2021). However, these mechanisms produce small black holes that make up $<1\%$ of the total mass of the cluster; thus the black holes found in UCDs are mostly far too massive to result from these processes without significant subsequent accretion that is unlikely outside a nuclear environment. Therefore, the detection of high mass fraction black holes in luminous GCs provides strong evidence that they are stripped nuclei. At the same time, as we discuss below, these high mass fraction black holes are not expected in all stripped nuclei.

Even before SMBHs were detected in UCDs, there was indirect evidence of their existence. Central black holes raise the velocity dispersion of stars near the center of the stripped nuclei, elevating the apparent dynamical mass-to-light ratio derived from integrated dispersion measurements relative to the expected mass-to-light ratio from stellar populations (e.g., Mieske et al. 2013; Forbes et al. 2014). The enhanced mass-to-light ratio was used by Mieske et al. (2013) to predict the central black hole mass in UCDs with integrated dispersion measurements; they found similar mass fractions in many objects to the SMBH detections from resolved kinematics

discussed above. More recently, Voggel et al. (2019) used the inflated mass-to-light ratio measurements to quantify the fraction of luminous GCs that have high mass fraction black holes (and thus are likely stripped nuclei) as a function of luminosity; they find that $\sim 20\%$ of luminous GCs at $10^6 L_\odot$ have evidence for black holes, rising to $>70\%$ at the highest luminosities. This implies that a significant fraction of massive black holes in the local universe may be present outside of galaxy nuclei, a finding also shared by recent works (Greene et al. 2020; Ricarte et al. 2021). We expect a majority of these black holes in stripped nuclei to reside in lower luminosity nuclei than those that have currently been dynamically confirmed. Dynamical detection of smaller black holes in Virgo is not possible with current technology; thus finding candidates of these lower-mass stripped nuclei in nearby galaxies is important.

In this paper, we focus on finding additional candidate luminous GCs that may be stripped nuclei and have inflated mass-to-light ratios. We use high-resolution spectroscopic data to derive internal velocity dispersion measurements and present size estimates for a new sample of luminous GC candidates around NGC 5128 (hereafter Cen A). These luminous GCs extend out to 150 kpc in Cen A’s halo and are compiled from the candidates of Voggel et al. (2020) and Hughes et al. (2021), making it the largest and most complete study of luminous GC velocity dispersions in the outskirts of Cen A. Using the velocity dispersions and sizes, we estimate the dynamical mass-to-light ratio of each luminous GC.

The paper is organized into six sections. In Section 2 we describe the sample selection and observations. Section 3 describes our method to obtain velocity dispersion and metallicities for our luminous GCs. In Section 4 we estimate radii and V-band luminosities, and then calculate mass-to-light ratios and black hole mass predictions in Section 5. Finally, we conclude in Section 6. Throughout this paper we apply a distance modulus for Cen A of $(m-M)_0 = 27.91$ mag, corresponding to a distance of 3.8 Mpc. We correct individual objects for foreground extinction; a typical Milky Way extinction value near Cen A is $A_V = 0.306$ mag (Schlafly & Finkbeiner 2011).

2. Sample Selection and Data Reduction

2.1. Sample Selection and Sample Completeness

Based on the catalogs of Voggel et al. (2020) (hereafter KV20) and Hughes et al. (2021), we have targeted 314 GCs and stripped nuclei candidates around Cen A’s halo out to a projected distance of ~ 150 kpc; $\sim 135'$. KV20 is a catalog of 614 luminous GC candidates in Cen A based on Gaia DR2, and Hughes et al. (2021) is catalog of 40,502 GC candidates around Cen A based on data from the Panoramic Imaging Survey of Centaurus and Sculptor (PISCeS) survey, combined with Gaia DR2 and NOAO source catalog data. Our targets span a much larger range of galactocentric distance in comparison with previous studies (e.g., Rejkuba et al. 2007).

In addition to the 314 targets from these catalogs, we have also selected two previously confirmed GCs in Cen A—*aat329848*, from Beasley et al. (2008), and *VHH81-5*, from Rejkuba et al. (2007)—to provide us with some repeat measurements for testing the robustness of our results. We also targeted four nuclear star clusters (NSCs) of known Cen A satellite galaxies (*KK197-NSC*, *ESO269-06*, *Dw1-NSC*, and *DW3* from Crnojević et al. 2014, 2016), and a diffuse cluster in

Cen A, “Fluffy,” which was found through visual inspection of PISCeS images, and whose radial velocity was presented in Voggel et al. (2020). Thus in total, we observed 321 candidate luminous GCs. Of these 321 objects, we were able to measure the radial velocity for 219 candidates, of which 165 also had measurable velocity dispersions (see Section 3.3). Based on the radial velocities, we identify 78 as being Cen A clusters, and we measure the velocity dispersion and mass-to-light ratios (Section 5) for 57 of these.

To quantify the completeness of our sample of luminous GCs around Cen A, we first look at the total sample of luminous GCs around Cen A in the literature. We use the compilation of velocity and Hubble confirmed GCs in Hughes et al. (2021) and make a magnitude cut of $g \leq 19.1$ to define a clean sample of luminous GCs. This cut corresponds to $g_0 = 18.8$ and $M_V \sim -9.5$ ($L_V \sim 5 \times 10^5 L_\odot$), and is the same cut used by KV20. We also confirm here 13 clusters from KV20 as Cen A GCs based on their radial velocities. Thus in total there are 118 clusters with $g \leq 19.1$ with confirmed radial velocities in the literature. Of these 118 GCs with $g \leq 19.1$, 27 have previous reliable velocity dispersion measurements (Harris et al. 2002; Martini & Ho 2004; Rejkuba et al. 2007), while in this work we present 36 new measurements as well as remeasuring dispersions in 10 objects. Thus in total, 63 of the 118 GCs with $g \leq 19.1$ now have reliable velocity dispersion measurements. We also measure dispersions for 9 Cen A GCs and 2 additional nuclear star clusters at $g > 19.1$. Also, in the calculation above we exclude the large number of dispersion measurements from Taylor et al. (2010) and Taylor et al. (2015), because the median signal-to-noise ratio (S/N) of their measurements is very low (2 for Taylor et al. 2015), well below the limit where we find we can reliably measure dispersions using similar high-resolution spectroscopy. Just a handful of their measurements have S/N in the range of the measurements we present here. Issues with both their published velocities and dispersions have been documented previously (Voggel et al. 2018, 2019), and we find additional issues that we identify below.

We can also estimate the total number of luminous GCs in Cen A based on our confirmation of KV20 candidates. The KV20 sample is a nearly complete catalog of new luminous GC candidates at galactocentric radii beyond 5.5 kpc. Figure 1 shows the results of how many of our observed targets are confirmed as Cen A clusters based on their radial velocities (see Section 3.3). Using these data for the different ranks of cluster candidates in KV20, we estimate there are a total of ~ 31 real Cen A GCs in the catalog, of which we have found 13 so far. Combined with previously identified clusters that likely form a complete sample at smaller radii, we estimate a total of ~ 136 total luminous GCs with $g \leq 19.1$ around Cen A.

Throughout this paper, we use photometry for our sources from the NOAO DR2 source catalog (Nidever & Astro Data Lab team 2020). This photometry in ugriz is derived from DECam observations, and appears to be more reliably calibrated and more complete than photometry from the same data presented in Taylor et al. (2017). Throughout this paper, we present magnitudes corrected for galactic extinction using Schlafly & Finkbeiner (2011).

2.2. Spectroscopic Data of Luminous GC Candidates

The observations of 321 GC candidates in Cen A were taken over several observing runs between 2017 February and 2019

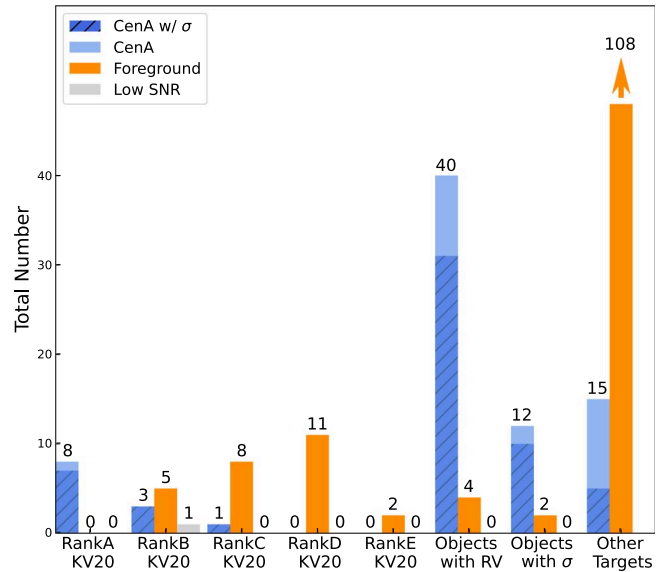


Figure 1. Histogram of 321 luminous GCs candidates in our sample categorized as Cen A Objects and Non Cen A Objects based on their radial velocities. We consider objects with $RV \geq 250 \text{ km s}^{-1}$ to be Cen A objects, while those with $RV \leq 250 \text{ km s}^{-1}$ respectively are likely Milky Way foreground stars (see Section 3.3 for details). RankA-E KV20 correspond to objects from the Voggel et al. (2020) catalog, with the A ranked objects being the highest likelihood to be GCs in Cen A. We also show objects with previous radial velocity and/or velocity dispersion (σ) measurements.

Table 1
Observation Log

Observation	Instr.	Setup	ExpTime (minute)	Seeing ($''$)	Obs Date mm/dd/yyyy
FieldMG 0	M2FS	Mg	4×45	0.65	02/24/2017
FieldMG 1	M2FS	Mg	4×45	0.9	05/20/2017
FieldMG 2	M2FS	Mg	4×45	1.2	05/21/2017
FieldMG 3	M2FS	Mg	4×40	0.77	05/30/2017
FieldMG 4	M2FS	Mg	4×48	0.8	06/03/2017
FieldMG 6	M2FS	Mg	3×50	1.1	05/11/2018
FieldCa 1	M2FS	Ca	3×40	0.7	02/26/2019
FieldCa 2	M2FS	Ca	3×67	0.7	03/01/2019
FieldCa 3	M2FS	Ca	3×34	0.7	03/04/2019
Night 1	MIKE	Full	180	0.85-1.02	06/17/2018
Night 2	MIKE	Full	270	0.7-1.2	04/05/2019
Night 3	MIKE	Full	405	0.8-1	04/06/2019

Note. Mg and Ca in column 3 refer to M2FS Magnesium and Calcium Triplets setup respectively. MIKE delivers full wavelength range coverage that includes Magnesium Triplet and Calcium Triplet and is denoted here as “Full” (see Section 2.2). Column 4 shows the number of exposures times the exposure time. For MIKE observations, each individual objects has a different exposure time, and we show only the combined exposure time.

March using the Michigan/Magellan Fiber System (M2FS) and the Magellan Inamori Kyocera Echelle (MIKE) spectrograph at the 6.5 m Magellan Clay telescope at Las Campanas Observatory, Chile. The list of M2FS plates and nights of MIKE observations are shown in Table 1.

M2FS is a fiber-fed double spectrograph optimized to operate from 3700–9500 Å (Mateo et al. 2012). Each spectrograph is fed by 128 fibers with a diameter of $1''2$. M2FS’s large field of view ($30'$ diameter) and its high spectral resolution ($R \simeq 25,000$; $\sim 10 \text{ km s}^{-1}$) are a perfect combination

to resolve the velocity dispersions of multiple GCs candidates simultaneously.

MIKE is a single slit echelle, double arm spectrograph, delivering full wavelength coverage from 3350–5000 Å (blue) and 4900–9500 Å (red) (Bernstein et al. 2003). We used a 1'' slit width to obtain a spectral resolution of $R \simeq 22,000$; $\sim 13 \text{ km s}^{-1}$ across the full wavelength range.

Our observation plan was to use M2FS for regions around Cen A where three or more high-priority luminous GC candidates (see below) are observable simultaneously, and target the rest of the high-priority candidates individually with MIKE. For targets observed with M2FS we used two distinct setups. First we observed using the MG_Wide filter, providing 4 orders ranging from 5119 to 5443 Å (hereafter Magnesium Triplet). We focused our analysis of these spectra on the second order spanning 5133–5218 Å, where the magnesium triplet lines (5167, 5172, 5183 Å) are located. The second setup uses the *CaIRT*₀₄₁ filter covering a single order 8471–8819 Å, which includes the “Calcium Triplet” lines at 8498, 8542, and 8662 Å. The Calcium Triplet setup provides higher S/N relative to the Magnesium Triplet but with stronger sky lines. These data allowed us to derive dispersions for fainter candidates. The MIKE data simultaneously provide full wavelength coverage from 3350–9500 Å. Our kinematic analysis of the MIKE data focused on the same regions studied with M2FS, specifically the Magnesium Triplet order covering 5140–5260 Å, and for the Calcium Triplet we use the order covering 8461–8708 Å.

The seeing for the observations was determined from the Las Campanas differential image motion monitor (DIMM) seeing monitor measurements during M2FS observations, and from direct measurements for the MIKE observations. The seeing is given in Table 1.

2.3. M2FS Data Reduction

The data reduction for M2FS was done using a combination of tasks in IRAF following the manual by Christian I. Johnson.⁹

The data reduction of the science frames requires a set of flat-fields, Thorium-Argon lamps, and bias frames for calibration. Each image observed with the CCD camera in M2FS is read out through four amplifiers that split the image into four frames. Each amplifier’s frame needs to be trimmed to remove the overscan region, bias subtracted, and rotated to be correctly oriented to join them into a single frame. We then remove cosmic rays from the combined images using the IRAF routine *L.A. cosmic*.

At this point the images are ready for data reduction with DOHYDRA. DOHYDRA is a sophisticated script optimized for the reduction of data from the Wisconsin Indiana Yale NAO (WIYN) and the Blanco Hydra spectrographs, but it can also be used for the data reduction of any similar multi-fiber spectrograph, such as the M2FS. The first step in DOHYDRA is the fiber identification using the luminous twilight spectrum in the flat-fields. For the Magnesium Triplet setup, each individual fiber has four orders on the detector; thus only 32 objects per plate are observable. For the Calcium Triplet setup, each fiber has only a single order, enabling observations of 128 separate objects per plate. For the Calcium Triplet we trace every fiber, because each fiber corresponds to a single target. For the Magnesium triplet we trace only the second order, because this

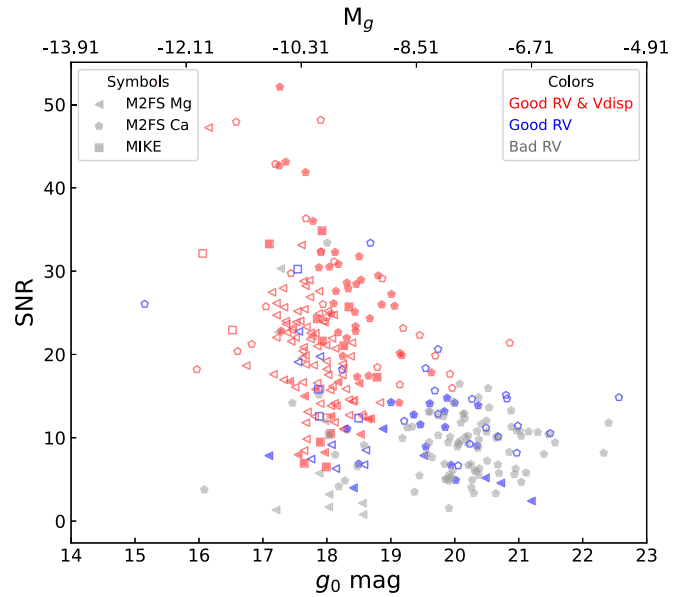


Figure 2. Summary of S/N and NOAO DR2 g magnitude for the 321 observed luminous GC candidates. We measure the S/N as the median of the S/N per pixel across the full wavelength range observed. We identify candidates observed with M2FS in the Magnesium Triplet with triangular markers and in the Calcium Triplet with pentagon markers, and targets observed with the MIKE Calcium Triplet with square markers. Red objects represent targets that have visually verified radial velocities and velocity dispersions, while blue objects have only visually verified radial velocities. Gray objects are targets for which we cannot obtain kinematic measurements. Solid and open markers represent targets with radial velocity consistent with Cen A or foreground stars respectively.

corresponds to the wavelength range with the Magnesium Triplet lines.

Typically flat-fielding would be performed next; however, we found that flat-fielding resulted in noisier spectra. For that reason we did not correct for the flat-fields, because accurate flux calibration is not important for our kinematic measurements. Finally, wavelength calibration was done using a Thorium-Argon (ThAr) lamp atlas (Palmer & Engleman 1983) to identify lines in the lamp frames. The typical rms of our wavelength solution was about a third of a pixel; the pixel size in the Calcium Triplet order is 0.11 Å, whereas for the Magnesium Triplet it is 0.06 Å. For the Calcium order data, the strong sky lines enabled us to check our wavelength solution—we find a standard deviation of the line wavelengths relative to expected of 0.076 Å, suggesting an absolute velocity error of $< 3 \text{ km s}^{-1}$. No sky subtraction was performed (instead we fit the sky during our kinematic fits; see Section 3.3).

After the data reduction with DOHYDRA was completed, we summed the spectra from multiple exposures into a single spectrum in Python for each object to increase the S/N. Additionally, DOHYDRA returns an error spectrum for each exposure. We summed in quadrature the error spectra of multiple exposures to create a single error spectrum.

A total of 301 targets were observed with M2FS, of them 116 in the Magnesium Triplet, and 185 in the Calcium Triplet setup. Our targets are brighter in the Calcium Triplet, providing significantly higher S/N than the Magnesium Triplet order. The 301 M2FS targets span a range of g absolute magnitude of -12.8 to -5.3 mag, with a median of -9.5 . Figure 2 shows the S/N ratio and g mag brightness for all our luminous GC candidates. For the five luminous GCs with large discrepancies between the NOAO DR2 and Gaia photometry (see Appendix),

⁹ <https://www.cfa.harvard.edu/oir/m2fsreduction.pdf>

we present estimated g -band magnitudes based on the median $g - V$ color ($g - V = 0.18$) of the rest of our luminous GC candidates.

2.4. MIKE Data Reduction

We observed 20 luminous GC candidates with MIKE, along with 22 known foreground stars on two nights from 2019 April 5–7 and on one night on 2018 June 16–17. The spectra were reduced with the CarPy reduction pipeline (Kelson et al. 2000; Kelson 2003). The pipeline automatically applies all the standard steps of applying the bias and flat-field to the data. In addition, it directly takes care of the sky subtraction as well as the rectification of the distorted spectra and cosmic ray removal.

The S/N for the MIKE Calcium Triplet data as a function of g -band magnitude is shown in squares in Figure 2. The 20 MIKE targets span a range of g absolute magnitude of -12.6 to -9.2 mag. Additionally, we had access to the fully reduced MIKE spectra of 14 luminous Cen A GCs from Martini & Ho (2004), used for testing our spectral fits (see Section 3.3).

3. Kinematic and Metallicity Measurements

3.1. Template Selection

We fitted the spectra of every candidate observed with M2FS and MIKE using the Penalized Pixel-Fitting pPXF routine (Cappellari 2017). pPXF requires a set of templates to model the spectra. We used the high-resolution ($R = 500,000$) synthetic stellar templates from the Phoenix library (Husser et al. 2013). We chose the temperature and $\log(g)$ of our Phoenix stellar templates based on the Padova Isochrones (Marigo et al. 2017) with an age of 10 Gyr, selecting stars along the subgiant, giant, and horizontal branch because these are expected to dominate the light of GCs. We selected templates with metallicities ranging from $[\text{Fe}/\text{H}] = 0.0$ to $[\text{Fe}/\text{H}] = -2.0$ with an interval of 0.5 dex, and $\log(g)$ from 0 to 4 with an interval of 0.5 dex. The temperature of the templates ranges from 3200–11,200 K. We note that we are not assuming a 10 Gyr age for our templates, but rather use a 10 Gyr isochrone to select the approximate $\log(g)$, metallicity, and temperature of the appropriate Phoenix templates because these properties determine the shape of the spectral lines of the templates. This resulted in a library of 46 total stellar templates.

3.2. Line-spread Function Determination

The synthetic stellar templates need to be convolved with the intrinsic line-spread function (LSF) of the observed spectra before fitting. We derive the LSF by fitting individual stars observed in each setup with our Phoenix templates using pPXF. We observed stars of known spectral type during the observing runs with MIKE, and those are used to determine the LSF. For M2FS, we did not observe stars of known spectral type, but many of our luminous candidate GCs were found to be Milky Way foreground stars based on their radial velocities ($V < 250 \text{ km s}^{-1}$). Assuming the spectrographs have Gaussian LSFs, the derived velocity dispersion for the stars measures the width of the intrinsic LSF of the instrument. The measured dispersion can be converted into FWHM (in Angstroms) $\text{FWHM} = 2\sqrt{2\ln(2)} \sigma_{\text{star}} \lambda_c / c$; with σ_{star} being the derived velocity dispersion, c the speed of light, and λ_c the central wavelength in each order. We used the median FWHM for all

the stars with S/N higher than 20 as the LSF (see Figure A1 in the Appendix). We obtained a different LSF for each filter (Calcium Triplet and Magnesium Triplet) and instrument. The error of the LSF was estimated by taking the standard deviation of the FWHM values, and this was propagated into the dispersion measurements later. The velocity dispersions measured in our luminous GC candidates are much higher than the width of the Gaussian LSF; therefore, the uncertainty in the LSF and errors caused by any non-Gaussianity of the LSF do not significantly affect our results.

3.3. Spectral Fitting

To ensure that our GCs are well fit by our selected templates, we optimized our pPXF parameters and template selection to maximize consistency with the velocity dispersion measurements of the 14 massive GCs from Martini & Ho (2004). Specifically, we removed two of our initial templates and set pPXF's multiplicative polynomial degree to 12. No additive polynomial was used to preserve relative line depths. Our pPXF fits were sensitive to the initial radial velocity guess, with objects with bad initial guesses often resulting in bad fits with unrealistically large dispersions. The initial radial velocity guess was obtained for each luminous GC candidate by running a grid of different radial velocity guesses from 0 – 900 km s^{-1} spaced by 100 km s^{-1} , and keeping the results from the fit with the best reduced χ^2 . Once a radial velocity guess was obtained, a bad-pixel mask was created by performing a 2σ clipping to remove outliers.

Because no sky subtraction was done during the data reduction for the M2FS data, for the Calcium Triplet M2FS data, we fit the sky emission lines with spectra from dedicated sky fibers in our field of view. After an initial fit, we examined the residuals at the wavelengths of known sky lines (Hanuschik 2003), and masked any pixels where the sky subtraction left significant residuals. For the MIKE data, sky subtraction along the slit was done during the data reduction; this also left behind sky residuals in some cases, and thus we apply the same masking procedure to the Calcium Triplet MIKE data. Our final radial velocity and velocity dispersion measurement pPXF runs use these initial radial velocity guesses and bad-pixel masks as input. An example of the fits for each setup is shown in Figure 3.

To estimate our errors on the radial velocity and dispersion measurements, we first recalculated the radial velocity and velocity dispersion using the lower and upper LSF values (see Figure A1), and then performed Monte Carlo simulations based on the error spectra for each object. Specifically, we added noise to the observed spectrum in every iteration based on its error spectrum and refit in pPXF. This was repeated 50 times for each object.

Figure 4 summarizes the radial velocity and velocity dispersion measurements for the 165 luminous GC candidates with measurable velocity dispersions. Based on previous spectroscopic studies (e.g. Peng et al. 2004), we use a radial velocity cut of 250 km s^{-1} to separate Cen A objects from possible foreground objects. Most targets with radial velocities lower than 250 km s^{-1} have significant ($>2\sigma$) Gaia EDR3 proper motions, and thus they are consistent with being Milky Way foreground stars. The target with radial velocity $\sim 230 \text{ km s}^{-1}$ (H12_82) has a significant Gaia EDR3 proper motion, suggesting it is a foreground star. High-velocity dispersion foreground objects are most likely binary stars;

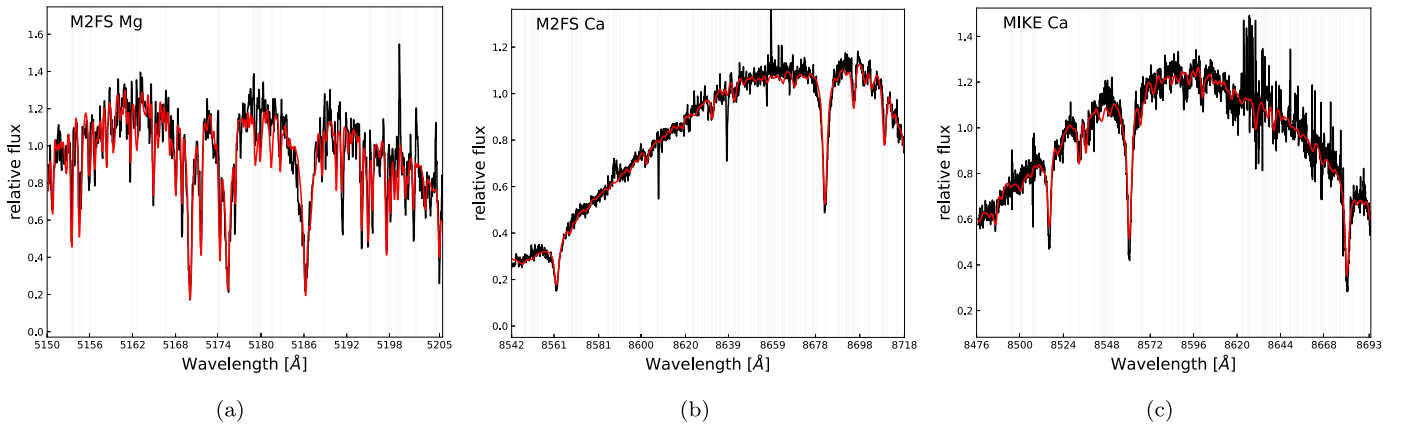


Figure 3. Spectral fit using pPXF examples for three luminous GCs in the M2FS Magnesium Triplet (M2FS Mg) (a), M2FS Calcium Triplet (M2FS Ca) (b), and MIKE Calcium Triplet (MIKE Ca) (c). The y-axis represents the relative flux per unit of wavelength. The observed spectrum (black) is fitted using the combination of stellar models (red). Gray vertical lines show masked regions including sky emission lines.

visual inspection shows double lines in many cases. None of the Cen A objects showed similar double line profiles.

3.4. Comparison to Literature and Reliability Assessment

Seventy of our luminous GC targets have literature radial velocity measurements (Peng et al. 2004; Woodley et al. 2005; Rejkuba et al. 2007; Beasley et al. 2008; Woodley et al. 2010). Out of these 70 targets, 13 have available velocity dispersions. Figure 5 shows the comparison of radial velocity measurements with literature values. We find a good agreement between the two with a scatter of 20 km s^{-1} and minimal bias. This scatter is in excess of reported velocity measurements in many cases. However, we think that this is a result of errors being underestimated in previous work; Beasley et al. (2008) found a 35 km s^{-1} offset and 60 km s^{-1} scatter in comparing their work to that of Peng et al. (2004). We reclassify four targets as foreground stars that were previously classified as Cen A GCs based on their radial velocities: these include two targets (*HH-32* and *AAT112964*) from Beasley et al. (2008) and one object from (*T17-1974*) Taylor et al. (2015).¹⁰

For the 13 luminous GCs with previous velocity dispersion measurements from Rejkuba et al. (2007), we can determine the velocity dispersion for nine of them. Their comparison with literature values is shown in Figure 6. The velocity dispersions of the 14 luminous GCs from Martini & Ho (2004) used to set up our pPXF fits (see Section 3.3) are shown in gray in Figure 6 because they are not part of the new measurements of luminous GCs presented here. We find a very good agreement with literature values, with a standard deviation of the residuals of 2 km s^{-1} , which is consistent with our velocity dispersion uncertainties. We do not include the $S/N < 5$ velocity dispersion measurements for *T17-1974* in Taylor et al. (2015), which was found to have a Milky Way foreground velocity.

The reliability of our dispersion measurements clearly correlates with S/N . However, due to varying positions of sky lines and outlier pixels in the spectra, a simple S/N cut did not cleanly separate good and bad measurements. For that reason, we visually inspected the shape and depth of multiple absorption lines in the fit for each luminous GC candidate to

determine if the fit was reliable; the kinematic fits passing this inspection are hereafter referred to as “visually verified” measurements. Figure 2 shows that our final visually verified dispersions are clearly correlated with S/N , with most spectra above S/N of 10 providing reliable dispersion measurements. We also find that almost all clusters with visually verified dispersions have $g_0 \lesssim 19$.

3.5. Repeated Measurements and Uncertainties

Many targets were observed with multiple setups (M2FS Magnesium Triplet and Calcium Triplet), or both with M2FS and MIKE. This allows us to do a comparison of their radial velocity and velocity dispersion to test any possible instrumental bias or differences between the Calcium Triplet and Magnesium Triplet measurements. The radial velocity comparison for 23 luminous GCs observed in both the Magnesium Triplet and Calcium Triplet is shown in Figure 7. We also included the 14 luminous GCs from Martini & Ho (2004) (see Section 3.3 for more details). For the Calcium Triplet radial velocities, we found a systematic offset toward higher values relative to Magnesium Triplet radial velocities. This systematic offset was 5.91 and 2.41 km s^{-1} for objects observed with M2FS and MIKE respectively; because we have no way of knowing which velocity is correct, we add these offsets as errors in quadrature with the Monte Carlo radial velocity errors for the two instruments.

In comparing repeat measurements, we found that our Monte Carlo errors for our velocity dispersion (see Section 3.3) were significantly underestimated. We therefore rescaled our errors based on these repeated measurements by fitting a Gaussian distribution to the difference of our repeated measurements normalized by their errors $((\sigma_{\text{Mg}} - \sigma_{\text{Ca}}) / \sqrt{\text{error}_{\sigma_{\text{Mg}}}^2 + \text{error}_{\sigma_{\text{Ca}}}^2})$. This gives us a scaling factor of 3.26 that we apply to all our velocity dispersion errors such that the repeated measurement differences normalized by the errors have a standard deviation of 1.

Three luminous GCs were observed with both M2FS and MIKE: *H12_78*, *KV19-271*, and *pff_gc-098*. These are shown in cyan in Figures 7 and 8—the x -axis position shows their MIKE calcium Triplet measurements. On the y -axis, for *KV19-271*, the Magnesium Triplet and Calcium Triplet M2FS observations are plotted separately, while for *H12_78* we use the M2FS Calcium Triplet value.

¹⁰ The previous velocities for these objects are 480 ± 27.4 for *HH-32*, $439 \pm 97.9 \text{ km s}^{-1}$ for *AAT112964*, and $503 \pm 8 \text{ km s}^{-1}$ *T17-1974*; our derived velocities are listed in Table 2.

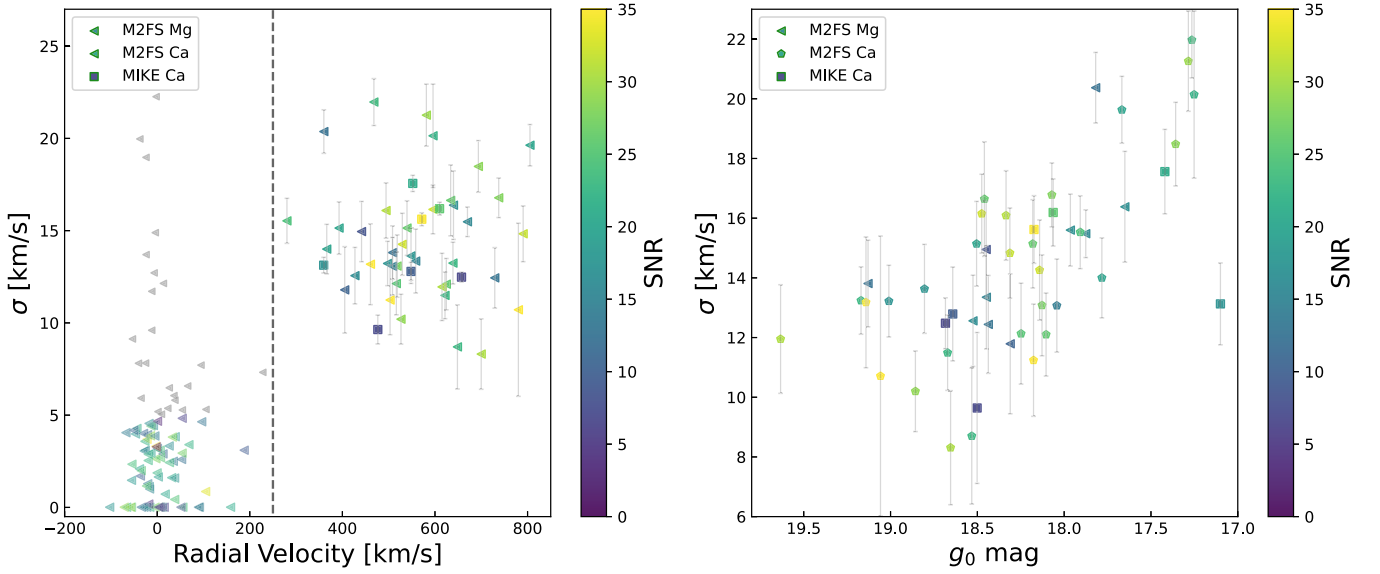


Figure 4. *Left:* radial velocity versus velocity dispersion for 165 luminous GC candidates with measurable dispersions. The black vertical dashed line shows the minimum radial velocity for Cen A GCs (250 km s^{-1}). Gray symbols show likely binary stars. *Right:* relation between g mag and velocity dispersion for the 57 luminous GCs with visually verified velocity dispersion. We expect a relation between these two quantities assuming that mass follows light, with brighter GC being more massive, and a $g \text{ mag} = 18.7$ corresponds roughly to a luminous GC mass of $10^6 M_\odot$ assuming a mass-to-light ratio of 2.

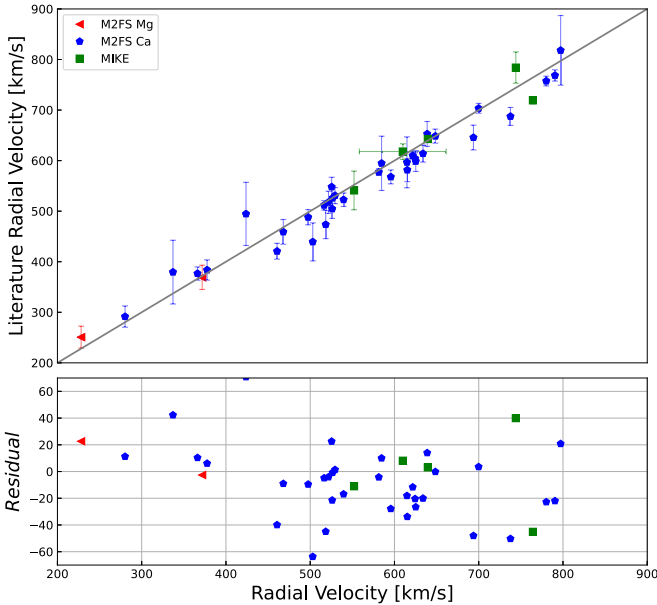


Figure 5. Comparison of 41 radial velocities in common between this work and values from the literature (Peng et al. 2004; Woodley et al. 2005; Rejkuba et al. 2007; Beasley et al. 2008; Woodley et al. 2010). The solid black line shows the one-to-one relation. Symbols represent the different configurations as described in Figure 4. The standard deviation of the residuals is 20 km s^{-1} .

Figure 8 shows the velocity dispersion comparison for the same 37 luminous GCs from Figure 7 observed in both the Magnesium Triplet and Calcium Triplet. We find a good agreement between the Magnesium Triplets' and Calcium Triplets' velocity dispersions, with a scatter of $\sim 2 \text{ km s}^{-1}$.

3.6. Metallicities

Using the weights of the templates used in the best fit from pPXF, we obtained a luminosity-weighted estimate of the metallicity of our luminous GC sample. The use of individual star templates (rather than Simple Stellar Population templates)

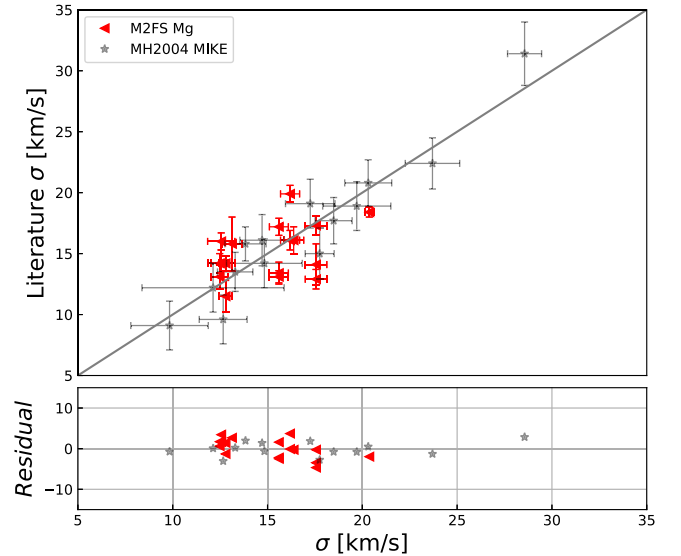


Figure 6. Comparison of 14 velocity dispersion estimates in common between this work and literature literature values from Harris et al. (2002), Martini & Ho (2004), Rejkuba et al. (2007), Taylor et al. (2010), and Taylor et al. (2015). The MH2004 MIKE data show the comparison with our analysis of the Martini & Ho (2004) data compared with their published values. The standard deviation of the residuals is 2 km s^{-1} .

and the known Age-Metallicity degeneracy for stars may lead to systematic uncertainties of the metallicity in some cases. For luminous GCs observed with MIKE where derived metallicities are available in the Calcium Triplet and also in the Magnesium Triplet (centered at $5127\text{--}5277 \text{ \AA}$), we present the error-weighted average metallicity between the two measurements.

To test the robustness of our metallicity estimates, we examine how they correlate with the measured colors from the NOAO photometry (Section 2.1), as well as metallicities for 31 of our luminous GCs inferred from Washington $C - T_1$ photometry from Harris et al. (2004). All 31 of these are

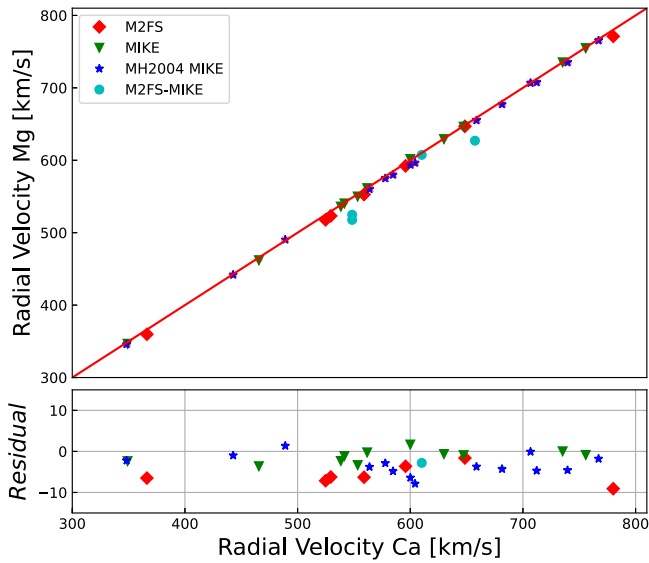


Figure 7. Comparison of 37 radial velocities for luminous GCs observed both in the Calcium Triplet and Magnesium Triplet. The red diamond and green inverse pyramids indicate GCs observed in both orders with M2FS and MIKE respectively. The MH2004 symbols indicate our rereduction of the MIKE data from Martini & Ho (2004), while the Cyan symbols indicate cross-instrument comparisons detailed in the text.

M2FS objects. These comparisons are shown in Figure 9. In the left panel we see the luminous GCs fall along the expected sequence, with lower metallicity objects being bluer, while higher metallicity are redder. In the right panel, the Harris et al. (2004) metallicity estimates are well correlated with our estimated metallicities—they have a Spearman coefficient of $r_{\text{spearman}} = 0.56$, suggesting that the correlation has a $>99\%$ significance, and a scatter of 0.32 dex. We have added this scatter in quadrature to the Monte Carlo errors in metallicity; these are the error bars shown in the right panel and listed in Table 2.

Outliers: In the right panel, we see two clusters lying at $(u - r)_0 \sim 2.4$ that fall far below the GC sequence and that have colors similar to foreground stars. Both objects (*K-029* and *HGHH-19*) have radial velocities consistent with being Cen A GCs ($638.8 \pm 5.9 \text{ km s}^{-1}$ and $621.7 \pm 5.9 \text{ km s}^{-1}$ respectively), and no significant Gaia EDR3 proper motions ($\lesssim 0.8 \text{ mas yr}^{-1}$). On the right panel, the largest outliers on the bottom right and top left (*T17-2078* and *HH-10*) are both located near the center of Cen A, and both show close companions that contaminate their photometry or spectroscopic measurement and compromise the derived metallicity. Based on these outliers, and the large scatter found in the right panel of Figure 9, we suggest caution in any future use of individual GC metallicities published here.

4. Radii and Luminosity Determination

In this section we discuss how we derived structural parameters and determine *V*-band luminosities for our sample of 57 luminous GCs with visually verified velocity dispersions. Structural parameters, in particular half-mass radii, are needed to derive virial masses. We then use the virial masses combined with *V*-band luminosities to estimate their mass-to-light ratios, which is the primary scientific goal of this work.

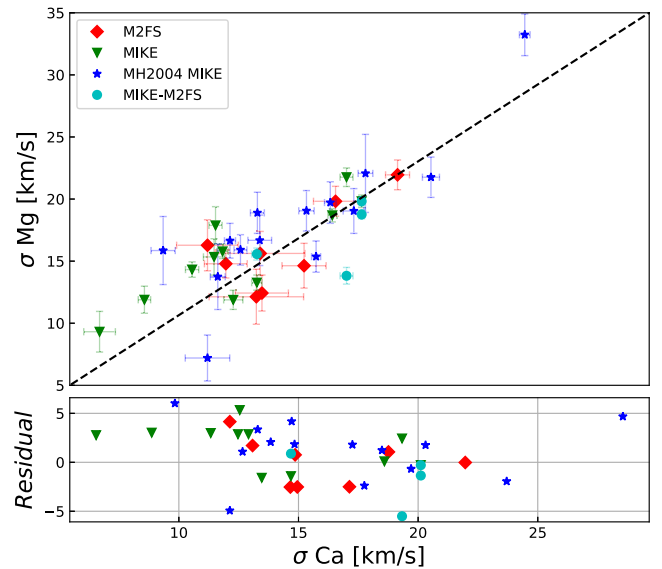


Figure 8. Comparison of 37 velocity dispersion measurements for luminous GCs observed in both the Calcium Triplet and Magnesium Triplet. Symbols are as described in Figure 7.

4.1. Radii Determination

Generally, half-mass radii are determined from the modeling of the light profile of imaging data, such as King models (King 1962, 1966) hereafter King62 and King66 respectively. At the distance of Cen A the typical GC half-light radius of 3 pc corresponds to just $0''.16$; thus high-resolution imaging is needed to estimate their sizes. Unfortunately, there is only archival high-resolution Hubble Space Telescope (HST) imaging data for 12 of our luminous GC candidates. We also have ground-based PISCeS imaging at the 6.5 m telescope Magellan Clay (Crnojević et al. 2016); although these data were taken in good seeing conditions ($\sim 0''.65$), they do not resolve the GC sizes, and modeling of the sizes from point-spread function (PSF) convolved-fits results in large errors in the inferred sizes.

For that reason, to determine the physical sizes of our GC candidates, we revisited the relation found in Voggel et al. (2020) between HST-based luminous GC sizes and the BP-RP Gaia excess factor (hereafter $\text{BR}_{\text{excess}}$). The $\text{BR}_{\text{excess}}$ is the ratio of the combined fluxes of the Blue-Pass (BP, 3300–6800 Å) and Red-Pass (RP, 6400–10500 Å) calculated in a window of $3''.5 \times 2''.1$, with the *G*-band flux determined from PSF fitting. (Gaia EDR3 has an effective angular resolution of $\sim 0''.4$; Fabricius et al. 2021.) The $\text{BR}_{\text{excess}}$ is sensitive to extended objects because the BP and RP are calculated over a larger area than the PSF photometry of the *G*-band. The $\text{BR}_{\text{excess}}$ is ~ 1 for point sources and larger for extended sources. We decided to use the newly available Gaia EDR3 catalog, instead of Gaia DR2 used in Voggel et al. (2020). Gaia EDR3 is more complete and thus has more sources with existing HST measurements for comparison. Additionally, the $\text{BR}_{\text{excess}}$ has also been recalibrated in Gaia EDR3 (Riello et al. 2021) relative to the Gaia DR2 values presented in Voggel et al. (2020); we also use half-mass radii here in place of half-light radii used in Voggel et al. (2020) to provide the inputs needed for virial masses.

To determine the relation between half-mass radius and $\text{BR}_{\text{excess}}$, we compiled a list of 71 half-light radii (r_h) and concentrations ($c = r_t/r_c$; with r_t and r_c being the tidal and core radii) of luminous GCs in Cen A derived from King66 model

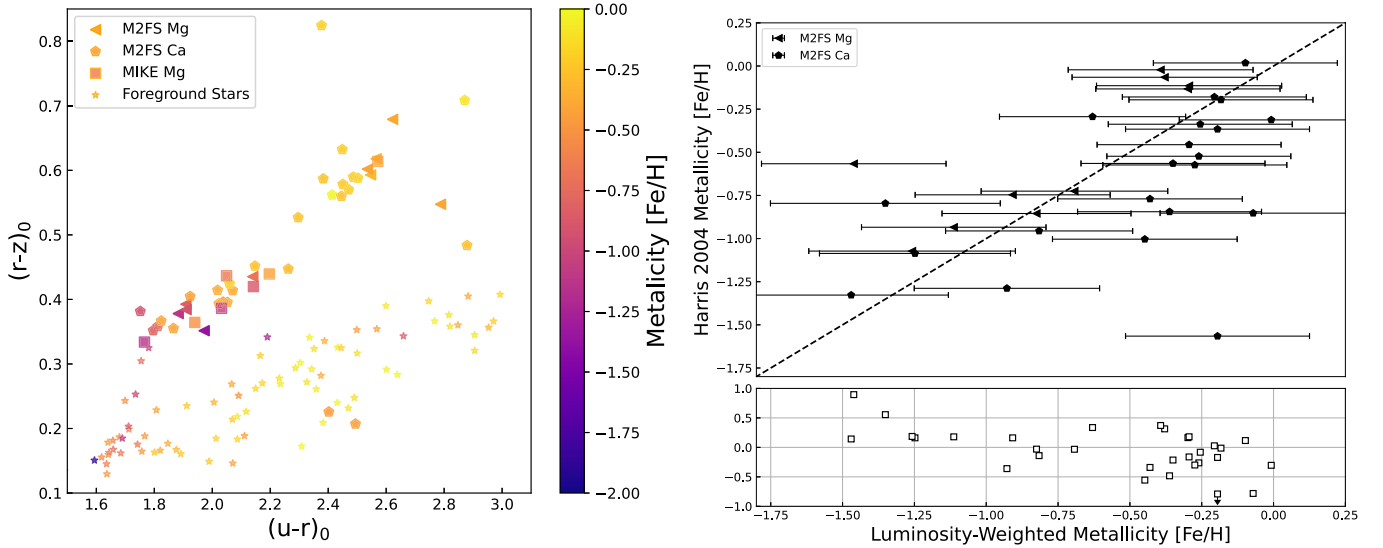


Figure 9. *Left:* $r-z$ vs. $u-r$ color plot for luminous GCs and Milky Way foreground stars colored by luminosity-weighted metallicities estimate. The triangles, pentagons, and squares represent targets observed with M2FS Magnesium Triplet, M2FS Calcium Triplet, and MIKE, respectively. *Right:* comparison of our flux weighted metallicities (x-axis) to derived metallicities (y-axis) for 31 luminous GCs using color information from the Washington photometric system from Harris et al. (2004). Symbols are as described above. The dashed black line shows the one-to-one comparison.

fits to HST images from McLaughlin et al. (2008). To convert their half-light radii to half-mass radii, we integrated King66 models for a range of concentrations to obtain the following relation:

$$r_{\text{hm}} = r_h(1.33592 - 0.05677 \log(c) + 0.03942 \log(c)^2 + 0.01146 \log(c)^3 - 0.00622 \log(c)^4) \quad (1)$$

The left panel in Figure 10 shows the resulting half-mass radii versus the measured Gaia $\text{BR}_{\text{excess}}$ colored by Gaia G magnitude. These two quantities show a strong positive correlation with a Spearman coefficient $r_{\text{spearman}} = 0.81$, suggesting that the correlation has a $>99.9\%$ significance.

We find a better recovery of the half-mass radii when including also a G -band magnitude dependence in the relation between half-mass radii and $\text{BR}_{\text{excess}}$. The resulting relation is shown in Equation (2).

$$r_{\text{hm}}('') = (0.08385 - 0.0086(G - 18))(\text{BR}_{\text{excess}} - 2.5) - 0.00785(G - 18) + 0.16135 \quad (2)$$

The right panel in Figure 10 shows the predicted half-mass radii for the sample of literature GCs. We find a fractional scatter of 14%, which is superior to the quality of ground-based sizes as well as the relation found in Voggel et al. (2020).

In this work we use half-mass radii from King66 fit to HST data when available (McLaughlin et al. 2008; Georgiev et al. 2009), and sizes from Gaia EDR3 from Equation (2) otherwise to calculate the mass-to-light ratios for our 57 luminous GCs. In addition three luminous GCs—*Fluffy*, *VHH81-5*, and *VHH81-01*—as well as galaxy nuclei *ESO269-06* were not in Gaia EDR3. For both *VHH81-5* and *ESO269-06*, HST ACS F606W imaging was available, and we fit King62 profiles (which are analytical) to determine half-mass radii and concentrations using a custom IDL routine that includes PSF convolution (as in Seth 2010). For *Fluffy*, due to its large size and resolution into individual stars, we created a 1D surface brightness profile from the HST WFC3 F606W, and fit this to a King62 model; this work will be presented in more detail in D. Crnojevic et al. (2022, in preparation). We demonstrate in

Section 5.2 that the differences between King62 and King66 profiles are negligible for the purposes of determining dynamical masses. Finally, for *VHH81-01*, no HST data was available; however, due to its large size, it was easily resolved in our ground-based PISCeS imaging. Using the r -band image, we fit the cluster with PSF convolution to a King66 model using *ishape* (Larsen 1999); the seeing of the r -band data was $0''.5$, significantly smaller than the $\sim 1/3$ half-light radius (See more details in Section 5.4).

4.2. V-band Luminosities

To make our mass-to-light ratios comparable to previous work, we derived V-band mass-to-light ratios. This required that we transform our extinction corrected NOAO Source Catalog DR2 aperture photometry (see Section 2.1) in u , g , r , and z into V-band using the photometric transformation: $V = g - 0.59(g - r) - 0.01$ from Jester et al. (2005). We compared the derived V-band magnitudes with previous V-band magnitudes for 185 GCs in Cen A from Peng et al. (2004) and Rejkuba (2001), and saw a slight bias of 0.087 mag toward brighter magnitudes in the NOAO DR2 photometry; this offset was constant with magnitude. Comparisons between Rejkuba (2001) and Peng et al. (2004) photometry suggest they are consistent; thus the offset appears to be related to a photometric calibration or aperture correction issue with the NOAO DR2 catalog. We note that available PISCeS photometry is saturated for many of our targets. We therefore use the derived V-band magnitudes derived from NOAO DR2 and subtract 0.087 mag to correct for this bias. For 10 objects we used HST imaging to obtain V-band magnitudes; these are detailed in Appendix.

For all 57 clusters, we calculated the V-band luminosities using $L_V = 10^{-0.4 * (V - (m - M)_V - A_V - M_{V,\odot})}$; we assumed $M_{V,\odot} = 4.81$ and $(m - M)_V = 27.91$ (i.e., distance of 3.8 Mpc) from Harris et al. (2010), and A_V was calculated using Schlafly & Finkbeiner (2011) for each object individually. The absolute V-band magnitudes M_V and $E(B - V)$ values used are listed in Table 3.

Table 2
List of All Observed Luminous GCs Candidates

ID	ID Ref	R.A. (deg)	Decl. (deg)	S/N	g_0 (mag)	R.V (km s ⁻¹)	R.V err (km s ⁻¹)	Metalicity (Fe/H)	Metalicity err (Fe/H)	Setup	Cen A?	Ref
GC_cand_37	This Work	200.926244	-43.565931	8.08	19.56	M2FS ca
GC_cand_38	This Work	200.959920	-43.543763	4.68	21.04	M2FS ca
T17-1027	Taylor2017	200.969649	-43.318745	4.91	20.01	502.0	7.1	-0.20	0.34	M2FS ca	Y	New
AAT301956	Beasley2008	200.977085	-43.333630	5.54	20.37	M2FS ca
H21-200841	This Work	200.979670	-43.463985	7.23	20.51	M2FS ca
GC_cand_0	This Work	200.989659	-42.868971	18.46	18.79	0.7	5.9	-1.03	0.32	M2FS ca	N	New
AAT101931	Beasley2008	200.993959	-42.954726	13.16	19.84	337.1	6.1	-1.31	0.36	M2FS ca	Y	RV
AAT102120	Beasley2008	200.998330	-42.922039	14.77	19.88	254.4	5.9	-1.49	0.33	M2FS ca	N	RV
AAT103195	Beasley2008	201.003257	-42.993677	11.31	20.89	M2FS ca
AAT103195	Beasley2008	201.024791	-43.065223	14.64	20.27	244.9	5.9	-0.15	0.32	M2FS ca	N	RV
AAT304867	Beasley2008	201.035856	-43.274220	10.10	20.17	M2FS ca
HH-131	Harris2004	201.065690	-42.886768	14.83	20.37	M2FS ca
KV19-235	Voggel2020	201.068541	-43.587734	29.73	17.44	-28.8	5.9	-0.57	0.32	M2FS ca	N	D
H12_322	Harris2012	201.073228	-43.444351	9.79	20.38	M2FS ca
HHH86-28	Hesser1986	201.075206	-42.816956	23.37	18.45	468.1	6.0	-0.82	0.33	M2FS ca	Y	RV
KV19-236	Voggel2020	201.076356	-43.344684	26.02	17.94	-24.2	6.0	-0.32	0.32	M2FS ca	N	C
KV19-237	Voggel2020	201.079546	-43.125361	16.37	19.14	26.0	6.0	-0.16	0.32	M2FS ca	N	D
HH-22	Harris2004	201.089178	-43.043633	30.51	18.04	615.2	5.9	-0.36	0.32	M2FS ca	Y	RV
HH-99	Harris2004	201.099886	-42.902972	14.11	19.61	614.8	6.0	-1.47	0.34	M2FS ca	Y	RV
KV19-239	Voggel2020	201.103008	-43.443754	33.39	18.00	M2FS ca
GC0025	Woodley2007	201.106419	-43.359877	12.76	19.36	797.2	5.9	-0.57	0.32	M2FS ca	Y	RV
H21-212899	This Work	201.106504	-43.553764	21.39	20.86	54.1	5.9	-0.57	0.32	M2FS ca	N	New
GC_cand_7	This Work	201.136470	-42.817503	12.11	...	17.8	5.9	-1.01	0.33	M2FS ca	N	New
GC_cand_9	This Work	201.141940	-42.890835	11.63	20.41	M2FS ca
GC_cand_40	This Work	201.144070	-43.461493	10.22	20.66	M2FS ca
GC_cand_45	This Work	201.154846	-42.280524	8.77	20.36	M2FS ca
GC_cand_8	This Work	201.156854	-42.885295	12.82	20.13	M2FS ca
H21-217713	This Work	201.158430	-43.607932	12.01	19.21	-1.2	6.0	-0.85	0.35	M2FS ca	N	New
GC_cand_1	This Work	201.166150	-43.134317	10.41	21.46	M2FS ca
GC_cand_39	This Work	201.166752	-43.465841	3.33	20.64	M2FS ca
H21-218792	This Work	201.170680	-42.870212	13.63	20.54	M2FS ca
KV19-248	Voggel2020	201.174218	-42.816574	48.13	17.90	13.4	5.9	-0.17	0.32	M2FS ca	N	D
GC_cand_42	This Work	201.179490	-43.247139	6.78	20.67	M2FS ca
HH-143	Harris2004_new	201.184850	-42.952465	14.33	19.98	M2FS ca
KV19-250	Voggel2020	201.188688	-43.666411	18.18	18.24	-146.2	16.0	-1.89	0.32	M2FS ca	N	E
HHH86-10	Hesser1986	201.200123	-43.137294	6.55	18.47	M2FS ca
T17-1253	Taylor2017	201.204815	-43.086707	17.83	19.63	548.3	5.9	-0.19	0.32	M2FS ca	Y	New
GC_cand_10	This Work	201.206403	-42.922385	14.84	22.57	26.1	6.0	-1.33	0.32	M2FS ca	N	New
H21-222371	This Work	201.209112	-43.167224	12.03	20.50	M2FS ca
H21-222450	This Work	201.209890	-43.700870	6.12	19.97	M2FS ca
GC_cand_3	This Work	201.210790	-43.055253	11.22	19.26	M2FS ca
GC_cand_4	This Work	201.222380	-43.051019	14.16	17.46	M2FS ca
AAT111185	Beasley2008	201.224886	-43.073512	14.18	20.00	297.6	6.4	-1.36	0.34	M2FS ca	Y	Sigma
GC_cand_2	This Work	201.225340	-43.163812	9.45	19.90	M2FS ca
HHH86-30	Hesser1986	201.226440	-42.890201	52.10	17.26	780.2	5.9	-0.01	0.32	M2FS ca	Y	RV
GC0450	Woodley2010	201.229040	-43.047889	10.77	20.35	M2FS ca
H12_320	Harris2012	201.236101	-43.091498	12.91	20.15	M2FS ca
GC_cand_5	This Work	201.240711	-42.875204	15.94	20.52	M2FS ca

Table 2
(Continued)

ID	ID Ref	R.A. (deg)	Decl. (deg)	S/N	g_0 (mag)	R.V (km s ⁻¹)	R.V err (km s ⁻¹)	Metallicity (Fe/H)	Metallicity err (Fe/H)	Setup	Cen A?	Ref
KV19-262	Voggel2020	201.242945	-42.990417	29.11	18.87	-5.0	6.0	-0.20	0.32	M2FS ca	N	D
pff_gc-026	Peng2004	201.243514	-42.714822	11.58	19.46	423.8	6.2	-1.25	0.33	M2FS ca	Y	RV
PFF-gc028	Peng2004	201.254757	-42.947666	25.99	18.86	539.6	5.9	-0.29	0.32	M2FS ca	Y	RV
HH-146	Harris2004_new	201.255640	-42.997411	12.57	19.82	M2FS ca
KV19-265	Voggel2020	201.257206	-43.018565	47.90	16.58	-2.8	6.0	-0.24	0.32	M2FS ca	N	C
HGHH-G066	Harris1992	201.263148	-43.050712	29.46	18.80	581.4	5.9	-0.21	0.32	M2FS ca	Y	RV
KV19-268	Voggel2020	201.267822	-43.654668	4.14	18.19	M2FS ca
AAT112964	Beasley2008	201.269131	-43.122756	15.65	19.69	38.3	6.1	-1.89	0.32	M2FS ca	N	RV
HGHH-43	Harris1992	201.269935	-43.160808	17.43	18.65	497.6	5.9	-0.43	0.32	M2FS ca	Y	RV
T17-1388	Taylor2017	201.270881	-42.954239	...	17.50	M2FS ca
HGHH-G342	Harris1992	201.274196	-42.983493	32.27	18.13	529.5	5.9	-0.26	0.32	M2FS ca	Y	RV
KV19-270	Voggel2020	201.279400	-43.589595	3.77	16.08	M2FS ca
H12_362	Harris2012	201.280990	-43.576428	6.83	20.25	M2FS ca
H21-229155	This Work	201.284580	-43.602688	9.99	20.65	M2FS ca
K-029	Kraft2001	201.288256	-42.983105	22.82	17.28	638.8	5.9	-0.43	0.32	M2FS ca	Y	RV
GC_cand_41	This Work	201.290160	-43.680682	7.65	19.64	M2FS ca
K-034	Kraft2001	201.292745	-42.892504	36.00	17.78	460.6	5.9	-0.20	0.32	M2FS ca	Y	RV
H12_312	Harris2012	201.293322	-43.389607	9.03	20.35	553.3	5.9	-0.38	0.33	M2FS ca	Y	New
HHH86-14	Hesser1986	201.293668	-42.747977	30.43	17.88	699.9	5.9	-0.26	0.32	M2FS ca	Y	RV
T17-1444	Taylor2017	201.299889	-42.953690	20.13	19.14	392.8	5.9	-0.51	0.33	M2FS ca	Y	New
H12_321	Harris2012	201.300813	-42.828038	13.88	20.37	422.3	5.9	-1.73	0.32	M2FS ca	Y	New
KV19-273	Voggel2020	201.304097	-42.989558	27.59	18.14	574.4	5.9	-0.42	0.32	M2FS ca	Y	C
GC_cand_6	This Work	201.307520	-42.906243	16.47	20.08	M2FS ca
H12_356	Harris2012	201.307530	-42.891987	10.81	21.02	M2FS ca
GC_cand_11	This Work	201.307884	-43.123905	13.14	19.61	M2FS ca
GC_cand_46	This Work	201.316690	-43.684997	5.81	21.11	M2FS ca
HHH86-33	Hesser1986	201.317717	-42.848127	28.94	18.53	526.6	5.9	-0.40	0.32	M2FS ca	Y	RV
HGHH-G219	Harris1992	201.322045	-42.979623	28.59	16.41	521.7	5.9	-0.30	0.32	M2FS ca	Y	RV
R253	Rejkuba2001	201.322105	-43.144183	10.29	19.74	M2FS ca
T17-1511	Taylor2017	201.327091	-43.021130	41.86	16.13	525.4	5.9	-0.26	0.32	M2FS ca	Y	RV
GC_cand_18	This Work	201.329656	-43.152162	10.54	21.49	-47.8	8.9	-1.08	0.37	M2FS ca	N	New
GC_cand_43	This Work	201.331820	-43.267958	8.27	20.85	M2FS ca
GC_cand_17	This Work	201.332360	-42.910364	11.79	22.40	M2FS ca
KV19-280	Voggel2020	201.334631	-42.985827	24.91	16.22	492.0	6.0	-0.35	0.32	M2FS ca	Y	B
KV19-281	Voggel2020	201.337980	-43.533540	17.65	19.92	-40.5	6.0	-0.14	0.32	M2FS ca	N	C
T17-1533	Taylor2017	201.339477	-43.324859	14.25	19.00	328.5	6.1	-1.79	0.33	M2FS ca	Y	New
GC0429	Woodley2010	201.345304	-43.136178	23.15	19.19	38.3	5.9	-0.14	0.32	M2FS ca	N	Sigma
HH-180	Harris2004_new	201.354510	-43.151349	9.24	20.06	M2FS ca
KV19-284	Voggel2020	201.357892	-42.986728	26.05	15.15	-8.7	5.9	-2.00	0.32	M2FS ca	N	D
KV19-286	Voggel2020	201.358467	-42.972696	...	16.51	M2FS ca
GC_cand_16	This Work	201.358769	-42.851680	11.43	20.99	-71.3	5.9	-1.15	0.37	M2FS ca	N	New
KV19-287	Voggel2020	201.368097	-42.775991	24.45	18.00	187.9	6.0	-0.47	0.32	M2FS ca	N	C
KV19-288	Voggel2020	201.369036	-42.941958	30.83	18.18	494.3	5.9	-0.41	0.32	M2FS ca	Y	A
WHH-17	Woodley2005	201.371848	-42.963098	28.44	18.46	693.7	5.9	-0.45	0.32	M2FS ca	Y	RV
H21-237144	This Work	201.373273	-43.612256	10.72	20.50	M2FS ca
WHH-18	Woodley2005	201.375285	-42.946367	31.76	18.50	790.5	5.9	-0.20	0.32	M2FS ca	Y	RV
HH-10	Harris2004	201.379309	-42.837526	42.67	17.25	503.0	5.9	-0.20	0.32	M2FS ca	Y	RV
KV19-289	Voggel2020	201.380317	-43.046136	43.11	14.63	640.1	5.9	-0.21	0.32	M2FS ca	Y	B

Table 2
(Continued)

ID	ID Ref	R.A. (deg)	Decl. (deg)	S/N	g_0 (mag)	R.V (km s ⁻¹)	R.V err (km s ⁻¹)	Metallicity (Fe/H)	Metallicity err (Fe/H)	Setup	Cen A?	Ref
HGHH-G359	Harris1992	201.385034	-42.980587	17.31	15.57	526.1	6.0	-0.63	0.32	M2FS ca	Y	RV
H12_106	Harris2012	201.386037	-43.560646	21.97	18.31	595.8	5.9	-0.35	0.32	M2FS ca	Y	A
PFF-gc056	Peng2004	201.386638	-42.940098	24.32	18.67	280.3	5.9	-0.93	0.32	M2FS ca	Y	RV
GC_cand_14	This Work	201.386687	-42.900866	18.34	19.54	101.6	5.9	-1.42	0.34	M2FS ca	N	New
GC_cand_13	This Work	201.390917	-42.832569	36.32	17.67	-19.5	6.1	-0.28	0.32	M2FS ca	N	New
T17-1637	Taylor2017	201.395080	-42.943318	12.33	20.16	M2FS ca
KV19-292	Voggel2020	201.396382	-42.808698	22.31	19.45	1.7	5.9	-0.10	0.32	M2FS ca	N	D
WHH-22	Woodley2005	201.397118	-43.091414	26.11	18.10	633.9	5.9	-0.35	0.32	M2FS ca	Y	RV
T17-1664	Taylor2017	201.407702	-42.941120	27.23	19.01	518.4	5.9	-0.23	0.32	M2FS ca	Y	RV
T17-1665	Taylor2017	201.408278	-43.283169	5.59	19.92	M2FS ca
KV19-295	Voggel2020	201.418464	-43.047600	19.89	19.17	805.2	6.0	-0.45	0.32	M2FS ca	Y	B
HHH86-34	Hesser1986	201.419139	-43.353852	22.79	18.45	648.5	5.9	-0.18	0.32	M2FS ca	Y	RV
GC_cand_48	This Work	201.420890	-43.628902	...	19.52	M2FS ca
HGHH-19	Harris1992	201.430768	-43.123036	22.64	18.18	621.7	5.9	-0.37	0.32	M2FS ca	Y	RV
KV19-296	Voggel2020	201.430918	-43.300956	32.27	17.91	-53.5	5.9	-0.12	0.32	M2FS ca	N	D
HGHH-35	Harris1992	201.434161	-42.983166	32.35	17.91	595.7	5.9	-0.27	0.32	M2FS ca	Y	RV
GC_cand_47	This Work	201.436130	-43.642691	5.46	19.45	M2FS ca
N21	Gomez2006	201.437940	-42.649436	6.69	20.21	M2FS ca
AAT119596	Beasley2008	201.441813	-43.140152	11.27	19.85	625.3	6.0	-1.34	0.35	M2FS ca	Y	RV
GC_cand_49	This Work	201.443400	-43.604783	8.18	22.33	M2FS ca
GC0590	Woodley2010	201.445670	-42.876120	4.83	19.91	M2FS ca
HGHH-G204	Harris1992	201.445728	-43.034851	27.90	18.33	737.7	5.9	-0.74	0.32	M2FS ca	Y	RV
HGHH-G251	Harris1992	201.452204	-42.961431	25.81	19.06	624.5	5.9	-0.26	0.32	M2FS ca	Y	RV
GC_cand_44	This Work	201.453510	-43.368077	10.65	21.30	M2FS ca
KV19-300	Voggel2020	201.461884	-42.950591	42.84	17.19	-57.7	5.9	-0.29	0.32	M2FS ca	N	D
GC_cand_21	This Work	201.469270	-43.083283	9.42	21.57	M2FS ca
GC_cand_50	This Work	201.471130	-43.541966	10.73	21.16	M2FS ca
GC0323	Woodley2007	201.472030	-42.514632	5.99	20.34	M2FS ca
GC_cand_22	This Work	201.474470	-42.995220	12.67	19.74	M2FS ca
GC_cand_23	This Work	201.477750	-43.131096	8.03	21.39	M2FS ca
H12_310	Harris2012	201.478079	-42.712559	4.02	20.26	M2FS ca
HH-107	Harris2004_new	201.485960	-42.979333	13.14	19.59	M2FS ca
H21-247341	This Work	201.486674	-42.499387	10.12	20.68	-45.7	5.9	-0.74	0.33	M2FS ca	N	New
GC_cand_15	This Work	201.490884	-42.918465	15.12	20.80	-26.8	6.5	-0.70	0.34	M2FS ca	N	New
pff_gc-080	Peng2004	201.498086	-42.544269	6.72	19.94	584.7	6.0	-1.35	0.40	M2FS ca	Y	RV
GC_cand_31	This Work	201.499810	-42.475312	11.33	19.33	M2FS ca
GC0479	Woodley2010	201.500000	-42.999472	10.21	21.04	M2FS ca
GC_cand_12	This Work	201.503270	-42.811023	11.80	20.10	M2FS ca
KV19-309	Voggel2020	201.519331	-43.482248	21.23	16.82	15.2	5.9	-0.41	0.32	M2FS ca	N	D
AAT122794	Beasley2008	201.519470	-42.793086	3.34	20.30	M2FS ca
H12_215	Harris2012	201.525480	-42.629742	9.12	18.58	M2FS ca
H12_327	Harris2012	201.526176	-42.719741	4.94	20.27	M2FS ca
H21-251200	This Work	201.527528	-42.869796	12.86	19.74	42.6	6.0	-0.00	0.34	M2FS ca	N	New
GC_cand_26	This Work	201.529580	-42.652576	6.04	20.31	M2FS ca
H21-251644	This Work	201.531996	-42.880424	20.63	19.74	-37.8	6.4	-0.88	0.33	M2FS ca	N	New
GC_cand_24	This Work	201.532449	-43.033752	19.85	19.70	-18.1	6.1	-0.97	0.33	M2FS ca	N	New
H21-252147	This Work	201.537507	-42.527812	15.96	19.96	-1.6	6.0	-0.97	0.32	M2FS ca	N	New
GC_cand_19	This Work	201.540110	-42.874367	10.88	20.97	M2FS ca
KV19-311	Voggel2020	201.543341	-42.521167	25.75	17.05	-50.4	6.0	-0.20	0.32	M2FS ca	N	C

Table 2
(Continued)

ID	ID Ref	R.A. (deg)	Decl. (deg)	S/N	g_0 (mag)	R.V (km s ⁻¹)	R.V err (km s ⁻¹)	Metallicity (Fe/H)	Metallicity err (Fe/H)	Setup	Cen A?	Ref
GC_cand_20	This Work	201.545560	-42.878286	9.37	20.05	M2FS ca
H21-253874	This Work	201.555566	-42.869355	14.69	20.82	-48.1	6.0	-0.40	0.36	M2FS ca	N	New
GC_cand_32	This Work	201.556733	-42.476640	9.26	20.23	-24.8	5.9	-2.00	0.32	M2FS ca	N	New
H12_301	Harris2012	201.557280	-42.658710	5.15	19.92	M2FS ca
GC_cand_27	This Work	201.560110	-42.826036	5.76	20.69	M2FS ca
HHH86-26	Hesser1986	201.563543	-42.808168	19.80	18.25	366.2	5.9	-0.10	0.32	M2FS ca	Y	RV
KV19-320	Voggel2020	201.580773	-42.625020	20.38	16.60	7.4	5.9	-0.43	0.32	M2FS ca	N	D
GC_cand_25	This Work	201.584800	-42.963931	8.93	20.04	M2FS ca
R118	Rejkuba2001	201.591612	-42.907344	6.85	19.84	M2FS ca
H21-257979	This Work	201.592922	-42.966858	9.42	20.20	M2FS ca
C51	Harris2004	201.600676	-42.783526	6.86	18.50	377.6	6.2	-0.07	0.32	M2FS ca	Y	RV
fl.GC-1	Harris2004_conf	201.609730	-42.815443	5.06	19.86	M2FS ca
H12_98	Harris2012	201.621990	-42.690375	11.07	18.32	519.6	5.9	-0.21	0.32	M2FS ca	Y	A
H12_300	Harris2012	201.626488	-42.675358	5.00	19.85	M2FS ca
KV19-325	Voggel2020	201.626726	-42.869731	4.86	18.28	M2FS ca
H12_229	Harris2012	201.644783	-42.677839	3.50	19.37	M2FS ca
HGHH-27	Harris1992	201.658290	-42.763861	4.08	23.42	M2FS ca
GC_cand_33	This Work	201.671910	-42.798656	6.31	20.38	M2FS ca
HH-100	Harris2004	201.710155	-42.843434	5.27	19.94	M2FS ca
GC_cand_29	This Work	201.712211	-42.493167	31.13	18.11	94.6	6.0	-0.39	0.32	M2FS ca	N	New
H21-274800	This Work	201.743124	-42.412481	8.18	20.97	-3.2	6.2	-0.89	0.33	M2FS ca	N	New
pff_gc-100	Peng2004	201.764180	-42.454757	25.09	18.44	516.6	6.0	-0.26	0.32	M2FS ca	Y	RV
GC_cand_30	This Work	201.765180	-42.609855	9.66	20.09	M2FS ca
GC_cand_28	This Work	201.780810	-42.462194	10.10	19.93	M2FS ca
GC_cand_36	This Work	201.783980	-42.742342	9.96	19.18	M2FS ca
H12_252	Harris2012	201.786313	-42.770891	8.93	19.55	665.5	6.3	-0.96	0.33	M2FS ca	Y	New
H21-281846	This Work	201.804760	-42.548015	13.25	20.88	M2FS ca
H12_194	Harris2012	201.824886	-42.494562	14.21	19.13	508.3	6.0	-0.35	0.32	M2FS ca	Y	New
H21-284161	This Work	201.825763	-42.490269	33.38	18.68	69.8	157.9	-0.03	0.32	M2FS ca	N	New
KV19-361	Voggel2020	201.871665	-42.796645	18.20	15.97	3.0	5.9	-0.28	0.32	M2FS ca	N	C
KV19-367	Voggel2020	201.886625	-42.464203	7.97	18.13	M2FS ca
H21-291979	This Work	201.897545	-42.590191	11.19	20.49	3.0	6.0	-0.14	0.32	M2FS ca	N	New
H21-294165	This Work	201.916844	-42.665642	10.21	20.21	M2FS ca
GC_cand_35	This Work	201.923990	-42.763798	5.62	20.93	M2FS ca
H12_259	Harris2012	201.926042	-42.546890	9.47	19.60	M2FS ca
GC_cand_34	This Work	201.951410	-42.532064	1.54	19.91	M2FS ca
H21-301067	This Work	201.980690	-42.662425	6.29	20.95	M2FS ca
H21-301709	This Work	201.986469	-42.636172	6.66	20.05	-1.3	6.1	-0.43	0.34	M2FS ca	N	New
KV19-386	Voggel2020	202.039586	-42.667068	15.17	17.87	M2FS ca
GC_cand_58	This Work	200.705866	-43.101057	14.14	18.12	-67.5	5.9	-0.08	0.32	M2FS mg	N	New
GC_cand_59	This Work	200.752432	-43.112764	3.19	18.03	M2FS mg
GC_cand_57	This Work	200.771436	-42.891460	1.68	18.03	M2FS mg
GC_cand_56	This Work	200.772643	-42.836061	22.04	17.51	-26.4	5.9	-0.07	0.32	M2FS mg	N	New
GC_cand_98	This Work	200.780177	-42.725442	16.06	17.50	-11.9	5.9	-0.10	0.32	M2FS mg	N	New
GC_cand_97	This Work	200.792280	-42.467880	7.44	17.75	5.3	6.0	-0.32	0.33	M2FS mg	N	New
GC_cand_99	This Work	200.793307	-42.710812	16.95	17.32	-17.1	5.9	-0.23	0.32	M2FS mg	N	New
GC_cand_103	This Work	200.826807	-42.720283	23.66	17.36	6.2	5.9	-0.05	0.32	M2FS mg	N	New

Table 2
(Continued)

ID	ID Ref	R.A. (deg)	Decl. (deg)	S/N	g_0 (mag)	R.V (km s ⁻¹)	R.V err (km s ⁻¹)	Metallicity (Fe/H)	Metallicity err (Fe/H)	Setup	Cen A?	Ref
GC_cand_104	This Work	200.827638	-42.603832	26.15	17.21	-24.0	5.9	-0.75	0.32	M2FS mg	N	New
GC_cand_96	This Work	200.833672	-42.470965	1.33	17.21	M2FS mg
GC_cand_102	This Work	200.838575	-42.504426	22.64	17.38	-19.2	5.9	-0.06	0.32	M2FS mg	N	New
GC_cand_108	This Work	200.855482	-42.625245	25.66	17.33	-43.3	5.9	-0.01	0.32	M2FS mg	N	New
T17-0962	Taylor2017	200.867583	-42.795075	...	16.76	M2FS mg
GC_cand_109	This Work	200.884594	-42.606130	27.94	17.31	-37.4	5.9	-0.00	0.32	M2FS mg	N	New
GC_cand_61	This Work	200.887129	-42.948218	15.89	17.89	-28.1	5.9	-0.04	0.32	M2FS mg	N	New
HH-32	Harris2004	200.909655	-42.773054	15.85	18.30	-16.4	5.9	-0.68	0.32	M2FS mg	N	RV
GC_cand_101	This Work	200.926014	-42.441631	23.23	17.47	6.7	5.9	-0.24	0.32	M2FS mg	N	New
HGHH-40	Harris1992	200.926391	-43.160493	11.08	18.88	371.8	5.9	-1.46	0.32	M2FS mg	Y	RV
VHH81-01	Berg1981	200.934030	-43.186620	16.77	17.42	640.0	5.9	-0.82	0.33	M2FS mg	Y	Sigma
GC_cand_66	This Work	201.001818	-43.039715	27.59	17.88	-2.7	5.9	-0.04	0.32	M2FS mg	N	New
GC_cand_67	This Work	201.009884	-43.038126	12.54	18.57	-34.3	5.9	-1.01	0.32	M2FS mg	N	New
GC_cand_114	This Work	201.017203	-42.476733	21.41	18.39	-11.7	5.9	-0.67	0.32	M2FS mg	N	New
GC_cand_100	This Work	201.017322	-42.425581	22.95	17.45	65.8	5.9	-1.25	0.32	M2FS mg	N	New
GC_cand_115	This Work	201.029323	-42.478151	22.18	17.77	-6.6	5.9	-0.06	0.32	M2FS mg	N	New
GC_cand_106	This Work	201.034219	-42.375900	21.56	17.44	-25.1	5.9	-0.66	0.32	M2FS mg	N	New
GC_cand_107	This Work	201.054692	-42.454430	25.20	17.54	-13.6	5.9	-0.16	0.32	M2FS mg	N	New
GC_cand_105	This Work	201.061614	-42.457369	28.80	17.63	-14.4	5.9	-0.06	0.32	M2FS mg	N	New
GC_cand_60	This Work	201.066234	-42.978155	12.01	17.97	M2FS mg
GC_cand_68	This Work	201.085209	-43.028346	11.81	17.67	-20.7	5.9	-0.33	0.32	M2FS mg	N	New
GC_cand_64	This Work	201.093532	-42.937789	6.77	18.58	-10.9	5.9	-0.52	0.32	M2FS mg	N	New
H12_67	Harris2012	201.100143	-43.386317	9.85	17.68	-36.2	5.9	-0.20	0.32	M2FS mg	N	New
GC_cand_65	This Work	201.106850	-42.987902	47.22	16.15	-21.9	5.9	-0.59	0.32	M2FS mg	N	C
GC_cand_113	This Work	201.121446	-42.424813	21.84	17.74	-2.4	5.9	-0.00	0.32	M2FS mg	N	New
GC_cand_112	This Work	201.130572	-42.397736	23.89	17.52	-4.1	5.9	-0.40	0.32	M2FS mg	N	New
H12_54	Harris2012	201.132246	-43.385425	20.40	17.62	17.3	5.9	-0.00	0.32	M2FS mg	N	New
GC_cand_62	This Work	201.137483	-42.891258	6.30	18.14	-43.7	5.9	-0.02	0.32	M2FS mg	N	New
H12_38	Harris2012	201.145898	-43.419643	17.62	17.16	-102.6	5.9	-0.47	0.32	M2FS mg	N	New
GC_cand_63	This Work	201.148937	-42.944297	21.12	17.99	-43.7	5.9	-0.32	0.32	M2FS mg	N	New
H12_34	Harris2012	201.151485	-43.394451	22.04	17.21	68.6	5.9	-0.22	0.32	M2FS mg	N	New
HGHH-41	Harris1992	201.162357	-43.335133	12.23	18.64	360.0	5.9	-0.40	0.32	M2FS mg	Y	Sigma
H12_64	Harris2012	201.162932	-43.412671	18.80	17.67	9.2	5.9	-0.29	0.32	M2FS mg	N	New
HHH86-29	Hesser1986	201.168230	-43.301482	12.58	18.06	729.2	5.9	-0.30	0.32	M2FS mg	Y	Sigma
H12_50	Harris2012	201.168389	-43.405788	24.03	17.58	4.2	5.9	-0.14	0.32	M2FS mg	N	New
HGHH-11	Harris1992	201.227938	-43.022712	5.74	17.88	M2FS mg
VHH81-03	Berg1981	201.242499	-42.936124	15.00	17.65	558.4	5.9	-0.29	0.32	M2FS mg	Y	Sigma
GC_cand_110	This Work	201.246411	-42.431244	19.09	17.55	50.8	5.9	-0.69	0.32	M2FS mg	N	New
HGHH-12	Harris1992	201.273697	-43.175240	8.24	17.96	441.4	5.9	-0.38	0.32	M2FS mg	Y	Sigma
T17-1412	Taylor2017	201.281782	-43.020912	15.82	17.82	670.2	5.9	-0.39	0.32	M2FS mg	Y	Sigma
GC_cand_111	This Work	201.295914	-42.467668	22.76	17.56	6.4	5.9	-0.26	0.32	M2FS mg	N	New
GC_cand_51	This Work	201.326213	-43.418236	18.40	18.26	-55.5	5.9	-0.25	0.32	M2FS mg	N	New
H12_37	Harris2012	201.334010	-43.207306	24.70	17.21	37.8	5.9	-0.30	0.32	M2FS mg	N	New
HGHH-44	Harris1992	201.382221	-43.322982	12.29	18.68	508.3	5.9	-1.11	0.32	M2FS mg	Y	Sigma
GC_cand_52	This Work	201.397008	-43.401533	14.10	17.89	89.1	5.9	-1.22	0.32	M2FS mg	N	New
H12_95	Harris2012	201.500890	-43.475899	16.70	18.17	902.3	5.9	-1.35	0.32	M2FS mg	Y	A
HGHH-25	Harris1992	201.511787	-42.949167	2.15	18.55	M2FS mg

Table 2
(Continued)

ID	ID Ref	R.A. (deg)	Decl. (deg)	S/N	g_0 (mag)	R.V (km s ⁻¹)	R.V err (km s ⁻¹)	Metallicity (Fe/H)	Metallicity err (Fe/H)	Setup	Cen A?	Ref
HGHH-07	Harris1992	201.522474	-42.942327	7.85	17.09	602.7	6.1	-0.91	0.34	M2FS mg	Y	New
HHH86-36	Hesser1986	201.532145	-42.866721	3.99	18.42	694.4	6.3	-1.26	0.36	M2FS mg	Y	Sigma
HHH86-37	Hesser1986	201.544021	-42.895178	0.78	18.56	M2FS mg
T17-1974	Taylor2017	201.566079	-42.916914	9.17	18.07	86.1	6.2	-1.08	0.33	M2FS mg	N	Sigma
GC_cand_54	This Work	201.584728	-43.261976	12.72	18.35	22.9	5.9	-0.03	0.32	M2FS mg	N	New
HHH86-38	Hesser1986	201.599020	-42.900292	10.41	18.53	405.1	5.9	-0.69	0.32	M2FS mg	Y	Sigma
GC_cand_53	This Work	201.609501	-43.229469	14.49	18.42	91.3	5.9	-0.29	0.32	M2FS mg	N	New
GC_cand_85	This Work	201.613929	-42.851094	13.84	18.15	34.9	5.9	-0.20	0.32	M2FS mg	N	New
GC_cand_55	This Work	201.627922	-43.467694	18.70	17.79	38.9	5.9	-1.09	0.32	M2FS mg	N	New
GC_cand_84	This Work	201.645428	-42.845629	11.03	18.26	12.6	5.9	-0.25	0.32	M2FS mg	N	New
T17-2078	Taylor2017	201.674724	-43.129189	7.96	17.55	228.1	5.9	-0.81	0.33	M2FS mg	N	RV
GC_cand_82	This Work	201.697685	-42.902040	20.99	17.85	158.5	5.9	-1.30	0.32	M2FS mg	N	New
H12_42	Harris2012	201.713064	-43.391586	24.00	17.35	55.5	5.9	-0.15	0.32	M2FS mg	N	New
GC_cand_83	This Work	201.747338	-42.846370	15.72	18.05	-8.1	5.9	-0.02	0.32	M2FS mg	N	New
H12_39	Harris2012	201.810932	-43.278301	30.31	17.28	M2FS mg
H12_80	Harris2012	201.829811	-43.283793	25.22	18.01	7.2	5.9	-0.11	0.32	M2FS mg	N	New
GC_cand_87	This Work	201.851621	-42.999337	22.54	17.82	-0.2	5.9	-0.33	0.32	M2FS mg	N	New
GC_cand_86	This Work	201.897707	-43.087222	11.06	18.27	-29.5	5.9	-0.56	0.32	M2FS mg	N	New
GC_cand_88	This Work	201.901736	-43.083001	8.52	18.61	36.0	5.9	-1.08	0.32	M2FS mg	N	New
GC_cand_70	This Work	201.916629	-43.212664	18.88	18.25	4.0	5.9	-0.11	0.32	M2FS mg	N	New
GC_cand_69	This Work	201.921895	-43.254038	14.36	18.40	-12.4	5.9	-0.08	0.32	M2FS mg	N	New
GC_cand_89	This Work	201.946089	-43.067028	18.23	17.99	-46.9	5.9	-0.07	0.32	M2FS mg	N	New
H12_82	Harris2012	201.993013	-43.443015	22.66	17.24	M2FS mg
GC_cand_71	This Work	202.001586	-43.322300	21.94	18.08	-15.9	5.9	-0.15	0.32	M2FS mg	N	New
GC_cand_92	This Work	202.014541	-42.847463	17.55	18.02	10.8	5.9	-0.02	0.32	M2FS mg	N	New
GC_cand_90	This Work	202.046173	-42.885030	12.55	17.81	52.7	5.9	-0.27	0.32	M2FS mg	N	New
GC_cand_93	This Work	202.049456	-43.003961	13.84	18.06	-34.9	5.9	-0.08	0.32	M2FS mg	N	New
GC_cand_95	This Work	202.070384	-43.001883	16.16	18.09	-25.8	5.9	-0.08	0.32	M2FS mg	N	New
GC_cand_94	This Work	202.070749	-43.022249	16.58	17.85	25.9	5.9	-0.32	0.32	M2FS mg	N	New
GC_cand_91	This Work	202.073686	-42.989262	11.84	18.12	105.3	5.9	-0.25	0.32	M2FS mg	N	New
GC_cand_75	This Work	202.083470	-43.327759	19.77	18.37	-38.1	5.9	-0.14	0.32	M2FS mg	N	New
GC_cand_74	This Work	202.084923	-43.263532	14.23	18.83	-20.5	5.9	-0.69	0.32	M2FS mg	N	New
GC_cand_73	This Work	202.086062	-43.247189	20.71	18.13	31.3	5.9	-0.22	0.32	M2FS mg	N	New
GC_cand_72	This Work	202.108435	-43.134846	27.46	17.14	-4.6	5.9	-0.36	0.32	M2FS mg	N	New
H12_141	Harris2012	202.112521	-43.267474	16.53	18.50	427.1	5.9	-0.91	0.32	M2FS mg	Y	New
GC_cand_76	This Work	202.113796	-43.583358	8.47	17.64	51.3	5.9	-0.43	0.32	M2FS mg	N	New
GC_cand_77	This Work	202.125409	-43.300774	24.76	18.10	-55.5	5.9	-0.15	0.32	M2FS mg	N	New
GC_cand_80	This Work	202.147715	-43.444444	33.13	17.60	104.7	5.9	-0.47	0.32	M2FS mg	N	New
GC_cand_79	This Work	202.151394	-43.144182	12.78	18.54	0.5	5.9	-0.06	0.32	M2FS mg	N	New
GC_cand_78	This Work	202.163200	-43.252491	19.57	17.61	5.8	5.9	-0.31	0.32	M2FS mg	N	New
GC_cand_81	107	202.218800	-43.538992	16.66	17.62	-17.6	5.9	-0.23	0.32	M2FS mg	N	New
GC_cand_119	This Work	202.425319	-41.932317	18.65	16.74	36.1	5.9	-0.09	0.32	M2FS mg	N	New
GC_cand_118	This Work	202.448192	-42.058635	20.86	17.64	54.3	5.9	-0.13	0.32	M2FS mg	N	New
GC_cand_117	This Work	202.465986	-41.890188	13.12	17.70	96.2	5.9	-0.14	0.32	M2FS mg	N	New
GC_cand_116	This Work	202.514518	-41.866283	19.76	17.89	-30.2	5.9	-0.22	0.32	M2FS mg	N	New
GC_cand_121	This Work	202.516108	-42.095004	25.43	17.65	-23.0	5.9	-0.11	0.32	M2FS mg	N	New
GC_cand_122	This Work	202.516587	-42.020768	22.58	17.75	-65.9	5.9	-0.02	0.32	M2FS mg	N	New

Table 2
(Continued)

ID	ID Ref	R.A. (deg)	Decl. (deg)	S/N	g_0 (mag)	R.V (km s ⁻¹)	R.V err (km s ⁻¹)	Metallicity (Fe/H)	Metallicity err (Fe/H)	Setup	Cen A?	Ref
GC_cand_120	This Work	202.542261	-41.827168	23.31	17.68	26.5	5.9	-0.06	0.32	M2FS mg	N	New
Dw1_gc1	Crnojević	202.542780	-41.904666	5.19	20.48	266.0	5.9	-1.39	0.32	M2FS mg	Y	New
Dw1_gc3	Crnojević	202.550340	-41.884030	2.41	21.20	261.6	6.2	-1.07	0.34	M2FS mg	Y	New
Dw1_NSC	Crnojević	202.558373	-41.892037	7.87	19.51	273.2	5.9	-1.71	0.32	M2FS mg	Y	New
GC_cand_124	This Work	202.562538	-41.830811	19.20	17.99	2.5	5.9	-0.17	0.32	M2FS mg	N	New
Dw1_gc2	Crnojević	202.576700	-41.890874	4.57	20.72	259.6	5.9	-1.13	0.35	M2FS mg	Y	New
GC_cand_126	This Work	202.652907	-42.018333	19.88	17.67	-13.4	5.9	-0.02	0.32	M2FS mg	N	New
GC_cand_123	This Work	202.711633	-41.896283	23.86	17.96	-54.5	5.9	-0.13	0.32	M2FS mg	N	New
GC_cand_130	This Work	202.745810	-41.946335	14.58	18.34	-22.5	5.9	-1.02	0.32	M2FS mg	N	New
GC_cand_129	This Work	202.753764	-41.926794	24.92	17.87	-34.3	5.9	-0.10	0.32	M2FS mg	N	New
GC_cand_127	This Work	202.780820	-41.922054	28.91	17.73	-71.1	5.9	-0.07	0.32	M2FS mg	N	New
GC_cand_131	This Work	202.782970	-42.008797	24.00	17.93	6.5	5.9	-0.13	0.32	M2FS mg	N	New
GC_cand_128	This Work	202.822320	-41.997500	26.89	17.73	53.8	5.9	-0.06	0.32	M2FS mg	N	New
GC_cand_133	This Work	202.890194	-42.035338	28.24	17.66	32.8	5.9	-0.39	0.32	M2FS mg	N	New
GC_cand_132	This Work	202.915151	-42.053034	17.53	18.24	37.6	5.9	-1.03	0.32	M2FS mg	N	New
ESO269-06	This Work	198.286770	-44.889356	24.28	16.54	744.0	2.4	-1.26	0.33	MIKE	Y	RV
KV19-054	Voggel2020	199.102140	-44.554587	10.35	18.04	MIKE
Fluffy	Voggel2020	199.545360	-44.157251	10.52	18.48	764.3	2.5	-1.79	0.39	MIKE	Y	RV
KK197-NSC	Georgiev2009	200.508563	-42.535357	21.61	18.00	639.7	2.4	-1.16	0.34	MIKE	Y	Sigma
KV19-212	Voggel2020	200.790847	-43.874458	34.85	17.92	571.5	2.4	-1.03	0.33	MIKE	Y	A
KV19-258	Voggel2020	201.223936	-44.931835	32.12	16.06	2.2	3.3	MIKE	N	C
KV19-271	Voggel2020	201.296298	-43.509212	9.49	17.90	548.3	2.4	-0.42	0.32	MIKE	Y	A
VHH81-5	Berg1981	201.317123	-42.882801	33.26	17.51	563.2	2.4	-1.38	0.32	MIKE	Y	Sigma
aat329848	Beasley2008	201.505241	-43.570995	21.05	18.26	552.0	2.4	-0.55	0.33	MIKE	Y	RV
H12_78	Harris2012	201.672201	-42.703936	6.50	17.99	657.3	2.4	-0.71	0.34	MIKE	Y	A
pff_gc-098	Peng2004	201.724630	-43.321592	25.70	18.34	609.9	2.4	-0.50	0.32	MIKE	Y	RV
KV19-397	Voggel2020	202.104797	-42.858302	22.93	16.52	-47.9	3.3	MIKE	N	D
KV19-424	Voggel2020	202.321726	-45.212909	52.44	15.30	-62.0	3.3	MIKE	N	E
KV19-442	Voggel2020	202.432394	-42.391404	6.93	17.65	476.5	2.4	-1.35	0.34	MIKE	Y	A
DW3	Crnojević	202.586867	-42.191885	17.26	18.79	359.6	2.4	-1.12	0.35	MIKE	Y	New
KV19-464	Voggel2020	202.645456	-44.666926	30.24	17.54	-20.0	3.7	MIKE	N	B
KV19-492	Voggel2020	202.862883	-42.611324	12.57	17.88	-46.0	3.6	MIKE	N	B
KV19-521	Voggel2020	203.050732	-41.300504	15.81	17.87	-48.9	4.9	MIKE	N	B
KV19-569	Voggel2020	203.478428	-42.362581	12.39	18.00	56.7	3.4	MIKE	N	B
KV19-573	Voggel2020	203.537185	-42.866560	12.36	18.50	-25.4	3.4	MIKE	N	B

Note. Column 1 shows the Discovery ID for the luminous GC candidates. For 133 targets that were based on preliminary versions of Voggel et al. (2020) and Hughes et al. (2021) and do not have literature names, we name them as *GC_cand* with numbers running from 1 to 133. Literature references for the target ID are from van den Bergh et al. (1981), Lauberts (1982), Hesser et al. (1986), Karachentseva & Karachentsev (1998), Harris et al. (2002), Peng et al. (2004), Woodley et al. (2007), Georgiev et al. (2009), Harris et al. (2012), Crnojević et al. (2014, 2016), Taylor et al. (2017), Voggel et al. (2020), and Hughes et al. (2021). Columns 3 and 4 show R.A. and decl. in J2000 respectively. The S/N is shown in Column 5. Column 6 shows the extinction corrected NOAO DR2 *g*-band magnitude for the target. Columns 7 and 8 the heliocentric radial velocity and its error respectively. Columns 9 and 10 show the derived luminosity-weighted metallicity and its error. Column 11 denotes the instrument and setup used in the observation, with *ca* and *mg* being the Calcium Triplet and Magnesium Triplet respectively. For targets observed with MIKE, only the Calcium Triplet measurements are shown in this table. Y in Column 12 denotes if the target has radial velocity expected for Cen A GCs ($RV > 250 \text{ km s}^{-1}$), N if it has radial velocity consistent with Milky Way foreground stars, and N/A if we cannot reliably determine its radial velocity. Column 13 shows the literature source of the target. A–E denote the likelihood rank of being a Cen A GC from Voggel et al. (2020), with A and E being more and less likely respectively. RV and Sigma denote if the target has previous literature measured radial velocity and velocity dispersion respectively from Harris et al. (2002), Peng et al. (2004), Martini & Ho (2004), Rejkuba et al. (2007), or Taylor et al. (2010, 2015). Finally, “New” denotes targets that are not in the KV20 catalog, and that have no previous literature kinematic measurements.

(This table is available in machine-readable form.)

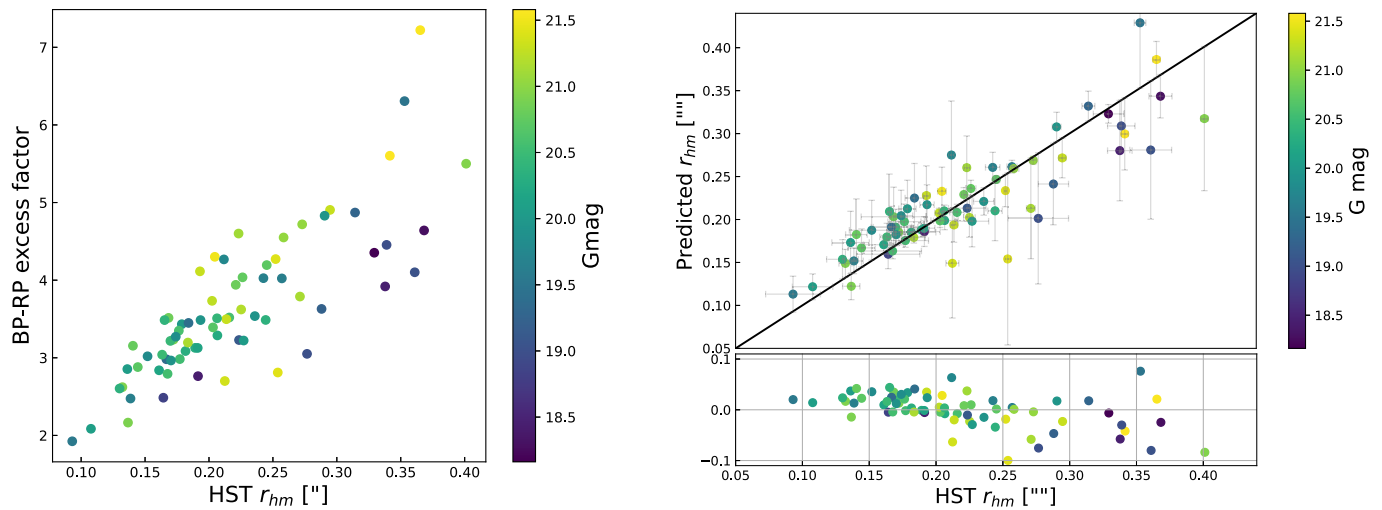


Figure 10. *Left:* a correlation is seen between the Gaia EDR3 BR_{excess} and the half-mass radii for Cen A GCs with available literature sizes from McLaughlin et al. (2008). *Right:* predicted half-mass radii for the same luminous GCs shown in the left using the fit to the correlation in the left panel given in Equation (2). This relation has a scatter of 14%.

5. Mass-To-Light Ratios

A primary goal of this work is to find potential stripped nuclei around Cen A that have elevated mass-to-light ratios that indicate the presence of a massive black hole (Mieske et al. 2013; Seth et al. 2014; Voggel et al. 2019). We use the velocity dispersion measurements combined with the half-light mass radii estimates from Section 4.1 to calculate each luminous GC’s virial mass using Equation (1) from Strader et al. (2009),

$$M_{\text{vir}} = \frac{7.5\sigma_{\infty}^2 r_{\text{hm}}}{G} \quad (3)$$

where σ_{∞} is the global velocity dispersion and r_{hm} is the half-mass radius (see Section 4), and G is the gravitational constant. At the distance of Cen A, luminous GC candidates are partially resolved from ground-based observations, resulting in the derived velocity dispersion being different from the global velocity dispersion (σ_{∞}). Due to the declining dispersion with radius in GCs, σ_{∞} will always be lower than our measured velocity dispersion. We calculate this difference by integrating a King66 profile convolved with the seeing over the spectrograph aperture of our observations as previously done in Strader et al. (2009). For clusters with Gaia estimated sizes, we assumed a concentration parameter $c = 30$, a typical value for Local Group GCs. The typical difference between the derived and global velocity dispersion is about 2% at $r_{\text{hm}} = 2.7$ pc, 5% at $r_{\text{hm}} = 4$ pc, and 7% for $r_{\text{hm}} = 7$ pc, with $1 \text{ pc} \approx 0''.05$. The maximum correction for any cluster in our sample was 15% for cluster *VHH81-01*, which has a half-mass radius of $1''.78$. Both our derived dispersion and the calculated σ_{∞} are listed in Table 3.

Figure 11 shows the V-band mass-to-light ratios (M/L_V) for our sample of 57 luminous GCs in Cen A. Also shown are GCs from M31 (Strader et al. 2011), UCDs from Virgo and Fornax compiled by Mieske et al. (2013), as well as literature objects from Cen A (Martini & Ho 2004; Rejkuba et al. 2007). Our mass-to-light ratios were computed by dividing the derived virial masses by the calculated V-band luminosities. For Cen A’s literature objects from Martini & Ho (2004) and

Rejkuba et al. (2007), we use updated half-light radii from McLaughlin et al. (2008) to revise the M/L_V estimates presented in the original papers. The half-light radii are then converted to half-mass radii (necessary to get M/L_V) using Equation (1). The list of clusters, half-mass radii, and their M/L_V values is shown in Table 4. As discussed in Section 2, we do not include objects from Taylor et al. (2010) and Taylor et al. (2015) in Figure 11 due to their typically low S/N. We also note that the half-light radii used in Taylor et al. (2015) are from unpublished work and are systematically larger than those presented by McLaughlin et al. (2008)—this would bias these values to higher M/L_V values than those presented in our work.

To investigate the M/L_V trends further, we plot their histogram in Figure 12 (blue-shaded region), revealing a bimodal distribution. We also show a kernel density estimate of the same data with a kernel width of 0.1 in red, while a similar kernel density estimate for the 45 M31 clusters with $M_V < -9.5$ from Strader et al. 2011 are shown in green. We choose to include only the brightest M31 clusters in this comparison to make the sample comparable in brightness to our Cen A clusters, and to reduce the impact of M/L evolution due to relaxation in the lower-mass clusters (e.g., Kruijssen 2008). The bulk of clusters in both samples have M/L_V between 1 and 2. However, in Cen A, the histogram as well as the comparison with M31 reveal a second population of clusters with an elevated $M/L_V \sim 3$. A Kolmogorov-Smirnov test gives a $>99.6\%$ significance that our observed distribution of M/L_V for luminous GCs in Cen A is different from those of M31 GCs. We also note that the high M/L_V population in Cen A is above the mean value of ~ 2.15 inferred by Voggel et al. (2019) from long relaxation M31 and Milky Way GCs and existing Virgo UCD measurements with black hole components removed.

To quantify the fraction of our luminous GCs with elevated M/L_V we used a Gaussian mixture model using the `sklearn` Python package.¹¹ After excluding the highest M/L_V cluster *VHH81-01* (our most massive and largest luminous GC; more details Section 5.4), we find that a Gaussian mixture model

¹¹ <https://scikit-learn.org/stable/modules/generated/sklearn.mixture.GaussianMixture.html>.

Table 3
List of 57 Luminous GCs with Visually Verified Velocity Dispersion

ID	R.V (km s ⁻¹)	R.V err (km s ⁻¹)	σ (km s ⁻¹)	σ err (km s ⁻¹)	σ_∞ (km s ⁻¹)	setup	r_{hm} ($''$)	r_{hm} Ref	M_V (mag)	$E(B - V)$ (mag)	M/L_V	BH Mass (M_\odot)	Ref
HH-22	615.2	5.93	13.07	1.82	12.44	M2FS ca	0.2498	Gaia	-10.18	0.108	1.25 ^{+0.44} _{-0.36}	...	RV
T17-1253	548.3	5.94	11.95	1.49	11.66	M2FS ca	0.1549	Gaia	-8.66	0.106	2.77 ^{+0.89} _{-0.73}	$1.12^{+0.9}_{-0.6} \times 10^5$	New
HHH86-14	699.9	5.92	15.48	1.91	14.12	M2FS ca	0.3407	M08/ACS	-10.39	0.109	1.81 ^{+0.79} _{-0.49}	...	RV
HHH86-30	780.2	5.91	21.97	4.69	20.97	M2FS ca	0.2352	Gaia	-11.02	0.106	1.54 ^{+0.82} _{-0.61}	...	RV
K-034	460.6	5.91	14.00	2.19	13.15	M2FS ca	0.3001	Gaia	-10.53	0.102	1.21 ^{+0.47} _{-0.39}	...	RV
PFF-gc028	539.6	5.92	10.20	1.48	9.90	M2FS ca	0.1768	Gaia	-9.40	0.101	1.15 ^{+0.41} _{-0.34}	...	RV
HHH86-28	468.1	5.97	13.35	1.27	12.68	M2FS ca	0.2557	Gaia	-9.75	0.122	1.98 ^{+0.54} _{-0.43}	...	RV
HGHH-G066	581.4	5.93	13.63	1.68	13.25	M2FS ca	0.1692	Gaia	-9.49	0.101	1.82 ^{+0.57} _{-0.47}	...	RV
HGHH-43	497.6	5.92	8.31	1.20	7.86	M2FS ca	0.2584	M08/ACS	-9.57	0.103	0.91 ^{+0.32} _{-0.27}	...	RV
KV19-273	574.4	5.93	14.26	1.65	13.37	M2FS ca	0.3118	Gaia	-9.59	0.100	3.12 ^{+0.96} _{-0.79}	$1.96^{+2.33}_{-0.96} \times 10^5$	C
HGHH-G342	529.5	5.92	13.08	1.68	12.49	M2FS ca	0.2321	Gaia	-10.07	0.100	1.30 ^{+0.42} _{-0.35}	...	RV
K-029	638.8	5.94	21.26	1.13	20.52	M2FS ca	0.1950	Gaia	-10.89	0.100	1.38 ^{+0.25} _{-0.22}	...	RV
HGHH-G219	521.7	5.91	14.83	1.33	14.25	M2FS ca	0.2101	Gaia	-9.42	0.099	2.79 ^{+0.69} _{-0.58}	$1.78^{+1.50}_{-0.78} \times 10^5$	RV
T17-1444	392.8	5.93	13.18	1.42	12.78	M2FS ca	0.1795	Gaia	-9.10	0.100	2.57 ^{+0.71} _{-0.61}	$1.24^{+1.14}_{-0.72} \times 10^5$	New
T17-1664	518.4	5.93	13.22	1.69	12.96	M2FS ca	0.1398	Gaia	-9.28	0.098	1.75 ^{+0.57} _{-0.46}	...	RV
HH-10	503.0	5.92	20.14	1.88	18.19	M2FS ca	0.5185	Gaia	-10.98	0.098	2.66 ^{+0.71} _{-0.61}	$3.22^{+6.65}_{-1.68} \times 10^5$	RV
HHH86-33	526.6	5.93	8.70	1.35	8.28	M2FS ca	0.2457	Gaia	-9.68	0.103	0.87 ^{+0.34} _{-0.27}	...	RV
PFF-gc056	280.3	5.92	11.49	1.22	11.06	M2FS ca	0.2086	Gaia	-9.52	0.099	1.53 ^{+0.42} _{-0.35}	...	RV
KV19-288	494.3	5.93	15.14	1.50	14.02	M2FS ca	0.3685	Gaia	-10.02	0.099	2.72 ^{+0.74} _{-0.63}	$1.90^{+2.81}_{-0.66} \times 10^5$	A
T17-1511	525.4	5.92	19.63	2.52	18.78	M2FS ca	0.1924	M08/ACS	-10.06	0.099	2.45 ^{+0.81} _{-0.69}	$2.38^{+3.35}_{-1.74} \times 10^5$	RV
KV19-280	492.0	5.95	16.78	1.08	16.26	M2FS ca	0.1785	Gaia	-9.66	0.099	2.47 ^{+0.50} _{-0.44}	$1.90^{+1.38}_{-0.84} \times 10^5$	B
HGHH-19	621.7	5.92	11.24	1.26	10.41	M2FS ca	0.3159	M08/ACS	-10.06	0.098	1.24 ^{+0.37} _{-0.31}	...	RV
WHH-22*	633.9	5.94	12.10	1.92	11.58	M2FS ca	0.1850	M08/ACS	-9.83	0.098	1.11 ^{+0.44} _{-0.35}	...	RV
KV19-295*	805.2	5.95	13.24	1.12	12.98	M2FS ca	0.1366	Gaia	-9.34	0.098	1.61 ^{+0.38} _{-0.32}	...	B
KV19-289	640.1	5.92	18.48	2.70	17.72	M2FS ca	0.2191	Gaia	-10.37	0.099	1.87 ^{+0.68} _{-0.56}	...	B
HGHH-G359	526.1	6.04	16.15	1.02	15.77	M2FS ca	0.1537	Gaia	-9.26	0.099	2.90 ^{+0.57} _{-0.51}	$2.20^{+1.02}_{-0.78} \times 10^5$	RV
WHH-17	693.7	5.92	16.64	1.40	16.11	M2FS ca	0.1832	Gaia	-9.95	0.099	1.90 ^{+0.44} _{-0.39}	...	RV
WHH-18	790.5	5.92	15.14	1.51	14.66	M2FS ca	0.1822	Gaia	-9.78	0.099	1.83 ^{+0.49} _{-0.51}	...	RV
HHH86-26	366.2	5.94	12.13	1.34	11.47	M2FS ca	0.2708	Gaia	-10.12	0.087	1.22 ^{+0.34} _{-0.30}	...	RV
HGHH-G204	737.7	5.92	16.09	1.07	15.26	M2FS ca	0.2574	Gaia	-9.85	0.098	2.62 ^{+0.54} _{-0.48}	$1.90^{+1.92}_{-0.78} \times 10^5$	RV
HGHH-35	595.7	5.92	15.53	1.32	14.93	M2FS ca	0.2114	Gaia	-10.30	0.098	1.36 ^{+0.34} _{-0.27}	...	RV
HGHH-G251	624.5	5.92	10.71	1.39	10.44	M2FS ca	0.1577	Gaia	-9.23	0.098	1.33 ^{+0.44} _{-0.35}	...	RV
pff_gc-100	516.6	5.96	12.44	1.69	11.91	M2FS ca	0.2233	Gaia	-9.86	0.099	1.38 ^{+0.48} _{-0.38}	...	RV
H12_194	508.3	6.02	13.81	1.56	13.33	M2FS ca	0.1947	Gaia	-9.10	0.096	3.02 ^{+0.90} _{-0.74}	$1.72^{+1.38}_{-0.84} \times 10^5$	New
HHH86-34	648.5	5.92	14.95	2.28	14.23	M2FS ca	0.2457	Gaia	-9.85	0.097	2.19 ^{+0.83} _{-0.68}	...	RV
H12_106	595.8	5.91	11.79	2.80	10.86	M2FS ca	0.3908	Gaia	-9.93	0.096	1.88 ^{+1.13} _{-0.85}	...	A
HGHH-41	360.0	5.92	12.79	1.18	11.90	M2FS mg	0.3233	M08/STIS	-9.66	0.115	2.39 ^{+0.37} _{-0.35}	$1.12^{+1.80}_{-0.36} \times 10^5$	Sigma
HGHH-12	441.4	5.92	15.60	1.63	14.81	M2FS mg	0.2462	Gaia	-10.35	0.106	1.49 ^{+0.23} _{-0.22}	...	Sigma
HHH86-29	729.2	5.92	16.19	1.64	14.90	M2FS mg	0.3628	M08/ACS	-10.25	0.112	2.46 ^{+0.39} _{-0.36}	$1.60^{+3.71}_{-0.36} \times 10^5$	Sigma
HGHH-44	508.3	5.94	12.48	1.45	11.93	M2FS mg	0.2642	M08/STIS	-9.52	0.099	2.23 ^{+0.35} _{-0.34}	$1.12^{+1.14}_{-0.54} \times 10^5$	Sigma
H12_95	902.3	5.93	15.62	1.20	14.92	M2FS mg	0.2318	Gaia	-10.05	0.090	1.88 ^{+0.29} _{-0.27}	...	A
VHH81-01	640.0	5.92	17.56	1.86	14.81	M2FS mg	1.7821	This Work	-10.80	0.118	7.17 ^{+1.14} _{-1.08}	$8.61^{+10.3}_{-0.12} \times 10^5$	Sigma

Table 3
(Continued)

ID	R.V (km s ⁻¹)	R.V err (km s ⁻¹)	σ (km s ⁻¹)	σ err (km s ⁻¹)	σ_∞ (km s ⁻¹)	setup	r_{hm} ($''$)	r_{hm} Ref	M_V (mag)	$E(B - V)$ (mag)	M/L_V	BH Mass (M_\odot)	Ref
VHH81-03	558.4	5.92	16.38	1.73	15.59	M2FS mg	0.2576	Gaia	-10.65	0.101	$1.32^{+0.21}_{-0.19}$...	Sigma
T17-1412	670.2	5.92	20.37	0.80	19.86	M2FS mg	0.1619	Gaia	-10.30	0.099	$1.85^{+0.26}_{-0.25}$...	Sigma
H12_141	427.1	5.91	9.64	1.53	9.07	M2FS mg	0.3021	Gaia	-9.70	0.093	$1.25^{+0.22}_{-0.20}$...	New
HHH86-38	405.1	5.93	12.56	2.34	12.19	M2FS mg	0.2172	Gaia	-9.72	0.087	$1.60^{+0.31}_{-0.27}$...	Sigma
aat329848	552.0	2.43	14.20	1.41	13.90	MIKE	0.2544	Gaia	-9.95	0.095	$1.96^{+0.29}_{-0.29}$...	RV
Fluffy	764.3	2.46	6.51	2.14	5.89	MIKE	1.6590	Crnojević	-9.67	0.093	$2.99^{+0.85}_{-0.71}$	$7.60^{+2.1}_{-3.0} \times 10^4$	RV
DW3	359.6	2.42	8.82	1.37	8.60	MIKE	0.2546	Gaia	-9.49	0.098	$1.15^{+0.20}_{-0.18}$...	New
ESO269-06	744.0	2.42	11.37	0.91	10.87	MIKE	0.3337	This Work	-9.88	0.081	$1.69^{+0.25}_{-0.24}$...	RV
pff_gc-098	609.9	2.42	14.93	1.12	14.62	MIKE	0.2028	Gaia	-9.92	0.093	$1.79^{+0.26}_{-0.26}$...	RV
KV19-212	571.5	2.42	19.38	1.13	18.84	MIKE	0.2725	Gaia	-10.33	0.111	$2.73^{+0.39}_{-0.39}$	$3.46^{+2.81}_{-0.9} \times 10^5$	A
KK197-NSC	639.7	2.42	12.91	1.33	12.55	MIKE	0.2111	G09/ACS	-9.80	0.133	$1.53^{+0.23}_{-0.22}$...	RV
VHH81-5	563.2	2.42	13.13	1.75	12.44	MIKE	0.7707	This Work	-10.63	0.101	$2.55^{+0.43}_{-0.40}$	$1.96^{+4.13}_{-0.54} \times 10^5$	Sigma
KV19-442	476.5	2.42	12.63	2.53	11.95	MIKE	0.4750	Gaia	-10.55	0.086	$1.57^{+0.31}_{-0.28}$...	A
H12_78	657.3	2.42	20.59	0.85	20.18	MIKE	0.2270	Gaia	-10.25	0.088	$2.82^{+0.39}_{-0.39}$	$4.59^{+2.4}_{-1.25} \times 10^5$	A
KV19-271	548.3	2.42	21.89	1.57	21.41	MIKE	0.2214	Gaia	-10.41	0.103	$2.65^{+0.39}_{-0.38}$	$4.47^{+2.76}_{-1.37} \times 10^5$	A

Note. Columns 1–3 are identical to Columns 1, 6, and 7 in Table 2. Columns 4, 5, and 6 show the derived velocity dispersion, its error, and the global velocity dispersions (see Section 5) respectively. In Column 7 are the calculated half-mass radii in arcseconds. Column 8 denotes the source of the calculated half-mass radii, with Gaia being the BR_{excess}-half-mass radii relation described in Section 4; M08/ACS and M08/STIS are sizes from McLaughlin et al. (2008). Column 9 shows the extinction corrected absolute V -band magnitude (assuming a distance modulus of $(m - M)_V = 27.91$). Column 10 shows the Galactic dust reddening used in column 9. Column 11 shows the calculated V -band mass-to-light ratio. Column 11 shows the predicted black hole mass necessary for luminous GCs with $M/L_V \geq 2.3$ to reproduce the observed elevated M/L_V . Column 13 is identical to column 13 in Table 2. We highlight (*) two luminous GCs with probably incorrect V -band luminosity (see Section 4).

(This table is available in machine-readable form.)

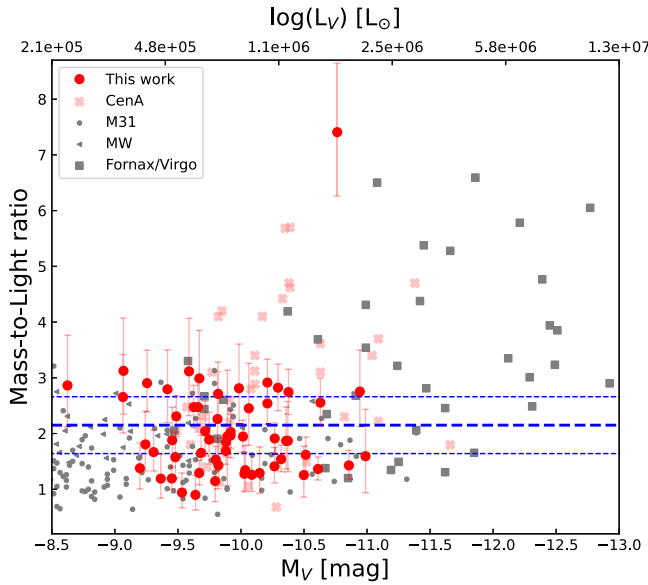


Figure 11. Luminosity of stripped nuclei and GCs compared with their M/L_V . Solid red circles are the 57 objects from this paper, while lighter red points are Cen A objects from the literature, and gray points are from other galaxies (see text for details). The horizontal dashed lines are the best fit and scatter of the stellar mass-to-light ratios of long relaxation systems from Voggel et al. (2019).

with 2 components best describes the observed distribution of M/L_V , with the lower M/L_V population peaking at $M/L_V = 1.51$ with a standard deviation of 0.32. The higher M/L_V peak is at 2.68 with a standard deviation of 0.21. The Gaussian mixture model suggests that 35.2% of our sample of luminous GCs (20/57) have an inflated M/L_V . This is the same as the number of objects that are above M/L_V of 2.3, which represents the dividing line where the probability of being in the lower and upper M/L_V population is equal. Relative to M31, we find $2.53\times$ more luminous GCs above M/L_V of 2.3.

One expectation from stellar models that is not borne out in observations is that the M/L_V should be metallicity dependent; this has also been found in previous work (Strader et al. 2011; Bruzual et al. 2013). We find no significant evidence of any trend of M/L_V with our derived metallicity (see Section 3.6) or PISCeS $g-r$ color. We note that for two objects, *KV19-295* and *WHH-22*, our M/L_V values may be incorrect due to bad $g-r$ colors used to estimate their V -band luminosity (see Appendix); their M/L_V values are 1.6 and 1.1, and thus both belong to the lower M/L population.

5.1. Nuclear Star Clusters

Our observations include four nuclear star clusters of present day galaxies. Of these, we were able to estimate mass-to-light ratios in three, *KK197-NSC*, *ESO269-06*, and *DW3*, from Crnojević et al. (2016). All three galaxies have total V -band luminosities of $<4 \times 10^7 L_\odot$ (Crnojević et al. 2019) and thus stellar masses of $\lesssim 10^8 M_\odot$. The nuclear star clusters have M/L_V of 1.13, 1.69, and 1.15 respectively, and thus none is consistent with being elevated and having high mass fraction black holes. Their virial masses range from $6 \times 10^5 M_\odot$ in *DW3* to $1.2 \times 10^6 M_\odot$ in *ESO269-06*. We note that *KK197-NSC* has a dynamical mass-to-light ratio estimate from Fahrion et al. (2020). We find a $\sim 3.5\times$ lower M/L_V than their published value of $M/L_V = 5.65 \pm 0.5$. This disagreement is due solely to their derived global velocity dispersion of $24.8 \pm 0.8 \text{ km s}^{-1}$ from

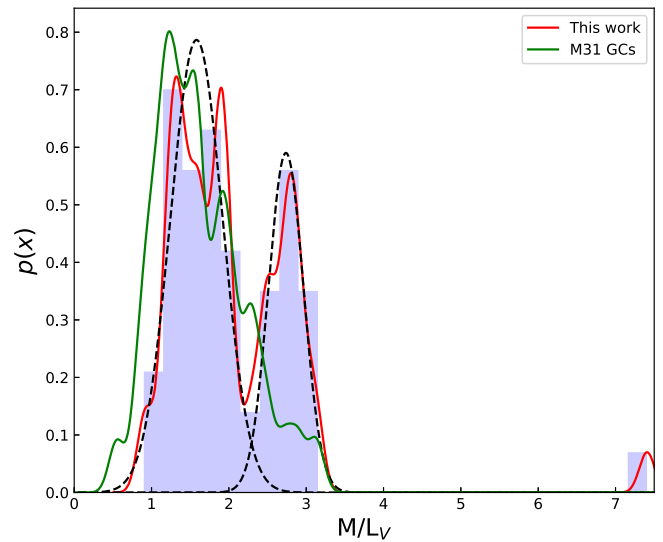


Figure 12. Histogram of the distribution of the M/L_V for the 57 luminous GC. A clear bimodality is seen in our data. A one-dimensional Kernel Density Estimation for our luminous GC is shown in red, compared with a similar estimate for M31 globular clusters (shown in green). The black dashed lines show the two mixture models for the best Gaussian mixture model for our luminous GCs. We find a clear bimodality with “normal” GCs peaking at $M/L_V = 1.51$, and luminous GCs with inflated M/L_V peaking at $M/L_V = 2.68$. The two populations are divided at $M/L_V = 2.3$. The outlier in M/L_V is our most massive luminous GC *VH81-01* (more details Section 5.4).

Very Large Telescope (VLT) Ultraviolet and Visual Echelle Spectrograph (UVES) data, which is a factor of $\sim 2\times$ higher than our global velocity dispersion of $12.5 \pm 0.4 \text{ km s}^{-1}$. For comparison we fitted the MIKE Calcium Triplet spectrum of *KK197-NSC* with a fixed velocity dispersion of 24.8 km s^{-1} from Fahrion et al. (2020). The fit has a reduced χ^2 of 1.48; this is 0.06 higher than our best fit reduced χ^2 of 1.42, a difference of more than 3σ . Additionally, the velocity dispersion measurement for the (lower S/N) MIKE Magnesium Triplet spectra of $15.3 \pm 4.3 \text{ km s}^{-1}$ is consistent with our best-fit MIKE Calcium Triplet velocity dispersion within the errors. We believe that the difference in velocity dispersion arises from the difference in extraction apertures. We use MIKE data with a $1''$ slit diameter and an optimal extraction with FWHM of $0''.81$. The extraction aperture in Fahrion et al. (2020) was significantly larger, $1''.2 \times 4''.0$, and thus may be dominated by the kinematics of the galaxy. Thus overall, we find that none of the nuclei has inflated mass-to-light ratios. Either these nuclei have no central black holes, or their black holes are lower mass than we can detect. As we show below, we can only detect black holes with $\gtrsim 10^4 M_\odot$ (or $\gtrsim 4\%$ of the cluster mass).

5.2. BH Mass Estimates for Luminous GCs

The population of high M/L_V objects could be due to the presence of massive black holes. This idea was suggested by Mieske et al. (2013), and the presence of black holes indicated by enhanced M/L_V values was verified in five high-mass UCDs in Virgo (Seth et al. 2014; Ahn et al. 2017, 2018; Afanasiev et al. 2018), as well as in the nuclei of galaxies (Pechetti et al. 2017; Krajnović et al. 2018). The finding of high mass fraction black holes in UCDs/luminous GCs is a strong indication of them being stripped galaxy nuclei. In this section we provide an estimate for the hypothetical central black hole (BH) mass for the 20 luminous GCs with elevated mass-to-light ratios ($M/L_V > 2.3$). The basic assumption we make here is that the

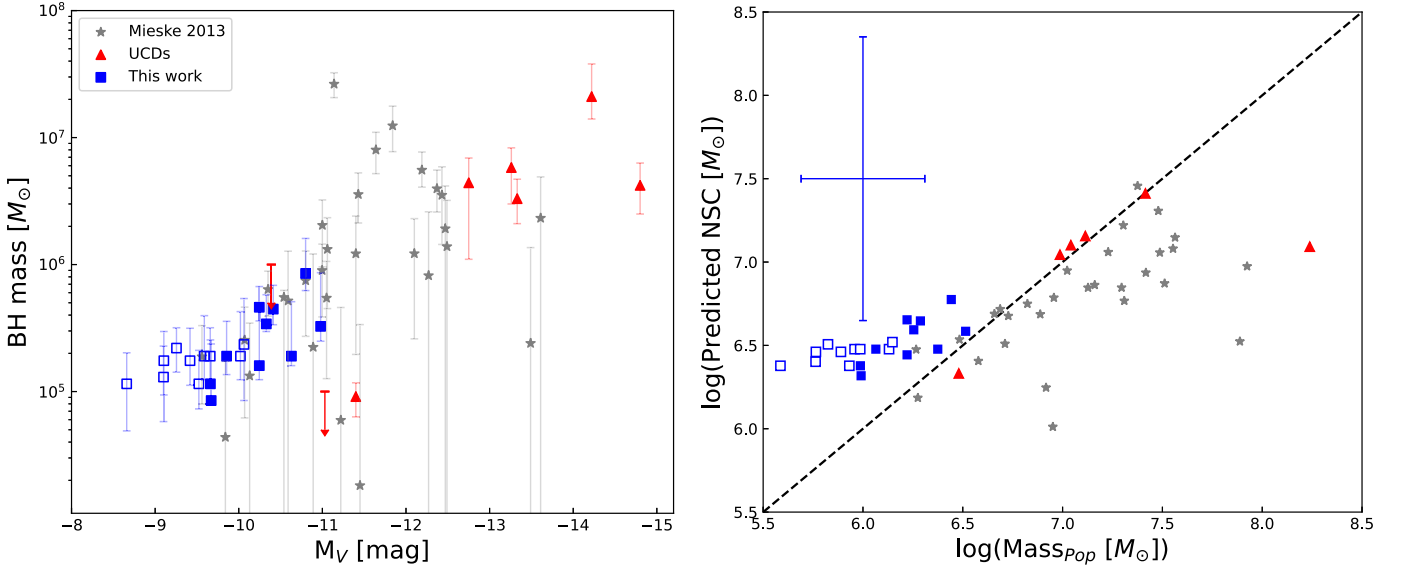


Figure 13. *Left:* predicted black hole masses for 20 luminous GCs in Cen A with inflated mass-to-light ratios versus their absolute V -band magnitudes (blue squares). Solid squares show luminous GCs with M/L_V enhancements $>3\sigma$, while open squares have less significant M/L_V enhancements. Gray stars are black hole mass predictions for stripped nuclei from Mieske et al. (2013). The five known black hole masses in UCDs from Seth et al. (2014), Ahn et al. (2017, 2018), and Afanasiev et al. (2018) are shown in red triangles together with two upper limits for two UCDs from Vogel et al. (2018) and the recent BH mass estimate from the most massive M31 globular cluster (B023-G078; $M_V = -11.4$) by Pechetti et al. (2022). *Right:* the X -axis shows the mass for 20 luminous GCs based on their V -band luminosity (L_V) from Table 3 assuming a $M/L_V = 1.51$ ($\text{Mass}_{\text{pop}} = L_V \times 1.51$). The Y -axis shows the predicted NSC mass based on the inferred black hole in the left panel using the empirical relation between black hole and total galaxy stellar mass (Reines & Volonteri 2015, Equation (4)) and total galaxy stellar mass and NSC mass (Neumayer et al. 2020, Equation (5)). The blue error bar indicates the uncertainty in both quantities: the vertical error bar is dominated by the scatter in the scaling relations, and the horizontal error bar is determined based on the width of the lower M/L_V component in Figure 12. Objects close to the one-to-one line (black dashed) are consistent with being stripped galaxy nuclei.

Table 4
List of Updated Mass-to-light Ratios for Literature Globular Clusters

ID	R.A. (deg)	Decl. (deg)	σ (km s $^{-1}$)	M_V (mag)	r_{hm} (pc)	M/L_V
HGHH92-C7	201.522542	-42.942333	21.10	-11.09	6.82	$2.22^{+0.07}_{-0.07}$
HGHH92-C11	201.228042	-43.022694	19.20	-10.35	10.67	$5.68^{+0.80}_{-0.75}$
HGHH92-C12	201.273833	-43.175194	13.10	-10.52	7.05	$1.49^{+0.19}_{-0.17}$
HGHH92-C17	201.415542	-42.933111	20.90	-10.63	7.41	$3.61^{+0.64}_{-0.58}$
HGHH92-C21	201.469750	-43.096222	19.00	-10.39	9.19	$4.62^{+0.48}_{-0.47}$
HGHH92-C22	201.473208	-42.985444	17.90	-10.11	4.99	$2.88^{+0.18}_{-0.17}$
HGHH92-C23	201.477417	-42.990389	30.50	-11.66	4.46	$1.79^{+0.14}_{-0.13}$
HGHH92-C29	201.168292	-43.301472	16.10	-10.11	6.68	$3.12^{+0.47}_{-0.42}$
HGHH92-C36	201.532208	-42.866750	15.70	-9.91	4.14	$2.21^{+0.74}_{-0.61}$
HGHH92-C37	201.544083	-42.895194	12.60	-9.83	3.04	$1.13^{+0.33}_{-0.28}$
HGHH92-C41	201.162417	-43.335111	11.50	-9.67	5.96	$2.13^{+0.75}_{-0.61}$
HGHH92-C44	201.382208	-43.322944	13.10	-9.57	4.87	$2.48^{+0.49}_{-0.44}$
HCH99 21	201.394375	-43.057694	10.60	-10.28	3.92	$0.68^{+0.34}_{-0.27}$
R223	201.386667	-43.117278	14.40	-9.49	3.09	$2.04^{+0.67}_{-0.55}$
R261	201.303750	-43.133083	14.60	-10.06	2.63	$1.06^{+0.27}_{-0.24}$

Note. Column 1 shows the name of the GC as identified in Rejkuba et al. (2007). Column 4 shows the derived velocity dispersion from Rejkuba et al. (2007). Column 5 shows the extinction corrected V -band absolute magnitude from Rejkuba et al. (2007). Column 6 shows the corresponding half-mass radii using transformation 1 with half-light radii from McLaughlin et al. (2008). Column 7 shows the updated V -band mass-to-light ratio. We calculated the mass-to-light ratio by taking the ratio of virial mass from Equation (3) using a central velocity dispersion based in values of Column 4 with the V -band luminosity from Column 5. For the central velocity dispersion we assumed a 6% correction between values of column 4 and σ_∞ based on the average correction by Rejkuba et al. (2007).

inflated M/L_V values are due to the presence of a black hole. We create dynamical models to derive the black hole mass required in each object assuming the true stellar M/L_V is given by the peak of the lower Gaussian mixture model component of 1.51 (see Section 5). This then provides a rough estimate of the masses of the possible black holes in these systems.

We first created a synthetic 1D King62 light profile for each object (due to the availability of an analytic expression for the King62 models). For objects with HST measurements, we used their corresponding concentration (c) and half-light radii, while for those where our half-light radii are from Gaia, we assume a concentration parameter $c = 30$. We then fit a Multi Gaussian

Expansion (MGE) model (Cappellari 2002) to the 1D King62 light profiles. Next, we use the MGE models as an ingredient in Jeans dynamical models (as implemented in the spherical version of the Jeans Anisotropic Modeling (JAM) software; Cappellari 2008). These models use the MGE light profiles of the clusters to predict the velocity dispersion within the observed aperture as a function of two free parameters: the stellar mass-to-light ratio and black hole mass. For this modeling, we assume the orbits of stars in the cluster are isotropic. Comparison of the predicted dispersion to the observed dispersion enables constraints on the mass-to-light ratio and BH mass. We note that without a black hole, the derived M/L_V for the clusters agrees extremely well with the virial mass measurements presented above (well within the 1σ errors), suggesting that the differences created by translating the effective radii and concentrations of King66 to King62 models are negligible. Next, we fixed the stellar mass-to-light ratio to 1.51, the mean M/L_V for clusters with lower M/L_V (see Section 5). Using this stellar M/L_V , we run a set of JAM models with a grid of increasing BH masses to simulate the effect of a BH on the integrated velocity dispersion. The BH mass that gives the closest velocity dispersion to the observed value is picked as the best BH mass. We obtained an upper and lower limit for the predicted BH mass using the errors in the M/L_V of each individual luminous GC.

The predicted BH masses versus their V magnitude are shown in the left panel of Figure 13, and their BH masses are listed in Table 3. We distinguish luminous GCs with significant BH mass predictions (BH mass $3\times$ above their lower error) with solid blue squares from less significant BH mass predictions (open blue squares). We also plot BHs determined in a similar way from Mieske et al. (2013). Our luminosity-BH relationship follows a similar trend to that found in Mieske et al. (2013), extending the predicted BH mass for luminous GCs down to M_V fainter than -9.5 ($M_V > -9.5$).

We find that BH masses of 4%–18% of the luminous GC virial mass (as calculated in Section 5) explain the inflated M/L_V that we observe, with a mean BH mass of $3.3 \times 10^5 M_\odot$ and a maximum BH mass of $8.61^{+10.3}_{-0.12} \times 10^5 M_\odot$ for the luminous GC VHH81-01, which we describe in more detail at the end of this section.

5.3. A Consistency Check for the Tidal Stripping Formation Scenario

We can test the plausibility of the stripped nuclei hypothesis by comparing the stellar mass of the clusters with a predicted NSC mass inferred from scaling relationships between black holes, NSCs, and their host galaxies similar to what was done in Graham (2020). If the luminous GCs with elevated M/L_V are the remnant stripped nuclei of galaxies, we expect their stellar mass to be comparable with the NSC mass of their progenitor galaxy (Pfeffer & Baumgardt 2013). We therefore use our inferred black hole mass in each cluster to predict the progenitor NSC mass and compare this with the observed cluster stellar mass. Because of the large scatter in the scaling relations, this test provides only an order of magnitude–level consistency check.

We estimate the cluster stellar mass based on their V -band luminosity with an assumed M/L_V of 1.51—the peak lower component of the Gaussian mixture model of Figure 12; we call this quantity Mass_{pop} . We use Mass_{pop} rather than a virial mass, because if these clusters do indeed have high mass fraction

black holes, our virial masses overestimate the stellar mass of the clusters. We then compare this mass with the NSC mass predicted based on the BH mass. To predict the NSC mass, we first infer the progenitor galaxy stellar mass based on the BH mass—total galaxy stellar mass from Reines & Volonteri (2015). A simple rearrangement of their Equation (4) with constants from their Equation (5) give us the following relation between galaxy stellar mass and BH mass:

$$M_* = 10^{\frac{\log(M_{\text{BH}}) - 7.45 \pm 0.08}{1.05 \pm 0.11}} \times 10^{11} [M_\odot] \quad (4)$$

where M_* is the galaxy stellar mass and M_{BH} the BH mass. Reines & Volonteri (2015) report a 0.55 dex scatter around this relation. The M_* is then translated back into an expected NSC mass using Equation (1) from Neumayer et al. (2020):

$$\log(M_{\text{NSC}}) = 0.48 \log\left(\frac{M_*}{10^9 M_\odot}\right) + 6.51 \quad (5)$$

with M_{NSC} being the NSC mass. Neumayer et al. (2020) report a 0.6 dex scatter around this relation. The comparison of the Mass_{pop} values and the predicted NSC mass are shown in the right panel of Figure 13. We calculated the errors in the predicted NSC mass by combining (in quadrature) the scatter of Equations (4) and (5). We find a good agreement between our Mass_{pop} and predicted NSC masses, with a mean difference of 0.11 dex for our significant BH predictions (those with 3σ M/L_V enhancements; these are shown as solid blue squares). This agreement is surprisingly good—the difference is much smaller than the scatter of relations from Reines & Volonteri (2015) and Neumayer et al. (2020). We also show data from similar measurements by Mieske et al. (2013) and literature UCDs with dynamical BH masses (Seth et al. 2014; Ahn et al. 2017, 2018; Afanasiev et al. 2018) and a recent BH mass estimate from the most massive M31 GC by Pechetti et al. (2022). For objects in Mieske et al. (2013), we estimated the NSC mass by multiplying their V -band luminosities with their M/L_V based on stellar population models for each individual object in Mieske et al. (2013). For the dynamical measurements, the stellar mass estimates on the y-axis are dynamically estimated based on the inner components of the UCDs. These show a rough agreement with the predictions with a few outliers including M59-UCD3 ($\log(\text{Mass}_{\text{pop}}) \simeq 8.2$) (Ahn et al. 2018).

We also made a similar comparison using the NSC mass—black hole mass relation derived by Graham (2020), who previously showed the good agreement between the BH masses and stellar masses for the UCDs with dynamical BH mass estimates. The Graham (2020) relation (their Equation (8)) combines the previous NSC–spheroid (Graham 2016) and black hole mass–spheroid (Scott et al. 2013) relationships to get a direct correlation between the NSC and BH masses. The agreement is not as good as using the total stellar mass relations above; we find the Mass_{pop} is on average 0.5 dex lower than the predicted NSC masses using the Graham (2020) relation for our significant BH detections. This discrepancy could be due to the extrapolation of the Scott et al. (2013) relation to lower BH masses than the galaxies it was based on, or simply due to the large scatter in this relationship (black hole masses have a range of ~ 2 dex at a given spheroid mass).

Overall, these comparisons support the idea that some of our luminous GCs are the remnant NSCs of stripped galaxies. We

stress here that these inflated mass-to-light ratio objects are likely just a subset of all the stripped nuclei around Cen A, because stripped nuclei could lack BHs or have BHs with mass fractions too small for us to detect.

As an alternative to central black holes, the inflated mass-to-light ratios could be due to tidal effects during stripping (Forbes et al. 2014). However, two points argue against this: (1) elevated mass-to-light ratios are seen in nearly a third of our luminous GCs, while inflated mass-to-light ratios due to tidal effects should be limited in duration and thus frequency, and (2) we see no trend of the fraction of luminous GCs with inflated mass-to-light ratios with radius. We find a mean galactocentric radius of 21.2 and 21.8 kpc for luminous GCs with inflated and non-inflated M/L_V respectively.

Another possibility is that the inflated mass-to-light ratios are due to variations from the canonical initial stellar mass function (IMF) in luminous GCs. Both top-heavy IMFs that would produce large numbers of stellar remnants (Dabringhausen et al. 2009) and bottom-heavy IMFs that would produce an abundance of low-mass stars (Mieske & Kroupa 2008) could explain the apparent high mass-to-light ratios. However, the dynamical detection of central SMBHs in massive UCDs (Seth et al. 2014; Ahn et al. 2017, 2018; Afanasiev et al. 2018) argues against these interpretations, because they show that the mass-to-light ratio clearly rises toward the center, and the outer mass-to-light ratio are consistent (or lighter than) predictions from stellar population models with standard IMFs. Additionally, a metallicity and density dependent IMF combined with a mass dependent BH retention fraction has been proposed to explain the M/L_V seen in UCDs (Jeřábková et al. 2017; Mahani et al. 2021). The mass segregation of the stellar mass BHs can produce a compact subcluster of BHs in lower-mass UCDs, such as those we discuss here, that raises their inferred M/L_V , although this mechanism cannot explain the central dispersion rises in the most massive UCDs ($>10^8 M_\odot$). Related work by Kroupa et al. (2020) suggests that a merger of the stellar mass BHs to form a central massive SMBH can occur at the centers of galaxies with spheroid masses $\gtrsim 10^9 M_\odot$; this threshold is close to the inferred spheroid masses in our sample of luminous GCs.

5.4. VHH81-01, a Very Massive Cen A Cluster

The cluster VHH81-01 has the highest mass-to-light ratio in our sample with $M/L_V = 7.16^{+1.16}_{-1.0}$, and also the highest predicted black hole mass. The virial mass estimate is $1.25 \times 10^7 M_\odot$, nearly identical to the Cen A cluster HCH99 18 from (Rejkuba et al. 2007), with a $M/L_V = 4.7^{+1.2}_{-1.6}$ (which they also suggest is a stripped galaxy nucleus). VHH81-01 has one of the two highest virial mass estimates of all clusters in Cen A.

VHH81-01 has literature velocity dispersion measurements from several sources (Rejkuba et al. 2007; Taylor et al. 2010, 2015). The Rejkuba et al. (2007) UVES dispersion is shown in Figure 6 and is 4.6 km s^{-1} lower than our derived dispersion of $17.6 \pm 0.8 \text{ km s}^{-1}$. While the UVES data Rejkuba et al. (2007) is higher resolution, their global dispersion of $12.4 \pm 0.8 \text{ km s}^{-1}$ agrees within the 1 sigma errors with our global dispersion of $14.8 \pm 1.8 \text{ km s}^{-1}$. Our derived dispersion agrees well with the values from Taylor et al. (2010), $15.9 \pm 1.6 \text{ km s}^{-1}$, and Taylor et al. (2015), $17.3 \pm 0.8 \text{ km s}^{-1}$. If we assume the $12.4 \pm 0.8 \text{ km s}^{-1}$ global velocity dispersion reported in Rejkuba et al. (2007) as the true value,

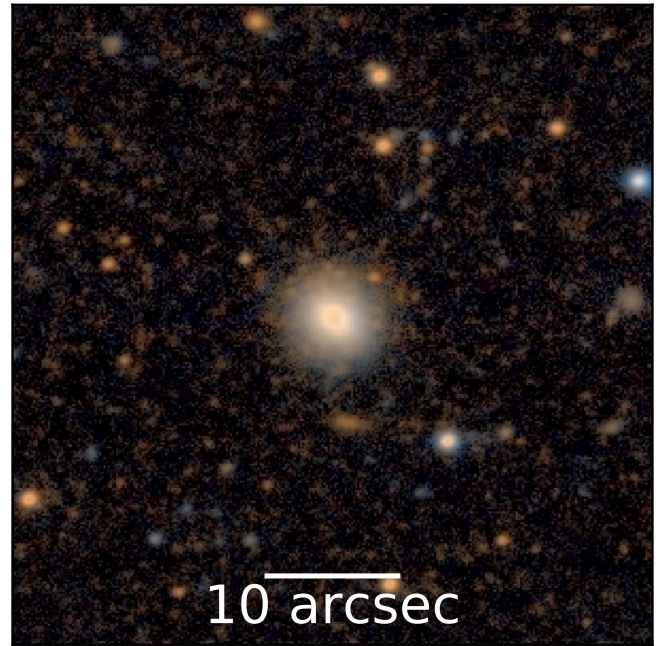


Figure 14. Color cutout of VHH81-01 from ground-based PISCeS imaging at the 6.5 m telescope Magellan Clay (Crnojević et al. 2016). The cutout is $0''.8 \times 0''.8$ in size, and oriented such that north is up and east is left.

we still get a high a mass-to-light ratio of $M/L_V = 4.91^{+0.63}_{-0.48}$ and a predicted BH mass of $4.96^{+1.51}_{-1.2} \times 10^5 M_\odot$, thus giving qualitatively similar results.

Our effective radius estimate of $1''.7$ (31.5 pc) derived from ground-based PISCeS imaging data (see Figure 14) is in good agreement with that from Taylor et al. (2015), which is from unpublished ground-based analysis by M. Gómez. Given the good seeing and large effective radius, we do not think that our size estimate could be falsely inflating the mass-to-light ratio. Furthermore we do not observe an unusual $g-r$ color for VHH81-01 that could underestimate its L_V and produce an inflated M/L_V . Therefore, it appears that this object truly has a high mass-to-light ratio and is the most likely of all of our objects to host a high mass fraction black hole.

In addition to VHH81-01, there are two other objects in Rejkuba et al. (2007), HGHH92-C11 and HGHH92-C21, that have similarly high M/L_V to VHH81-01. All three of these objects are highly flattened, with ellipticity $\gtrsim 0.25$ (greater than any MW GCs). We know that many nuclear star clusters are quite flattened, both in late-type galaxies and in massive early types (Seth et al. 2006; Spengler et al. 2017; Neumayer et al. 2020). HGHH92-C21 has an upper limit in the black hole mass of $1 \times 10^6 M_\odot$ from Voggel et al. (2018) (published there as UCD320), corresponding to a BH mass fraction of 38%. Voggel et al. (2018) also found a much lower M/L than previously published work due to a smaller derived effective radius for HGHH92-C21.

6. Conclusions

In this paper we present new high-resolution spectral data from M2FS and MIKE for 321 luminous GC candidates around Cen A. Of the 321 luminous GC candidates we can reliably determine the radial velocities for 219. Based on their radial velocities, we discover that 78 luminous GCs are members of Cen A, of which 27 are new discoveries. Of these 78, we can reliably measure the velocity dispersion of 57, including first

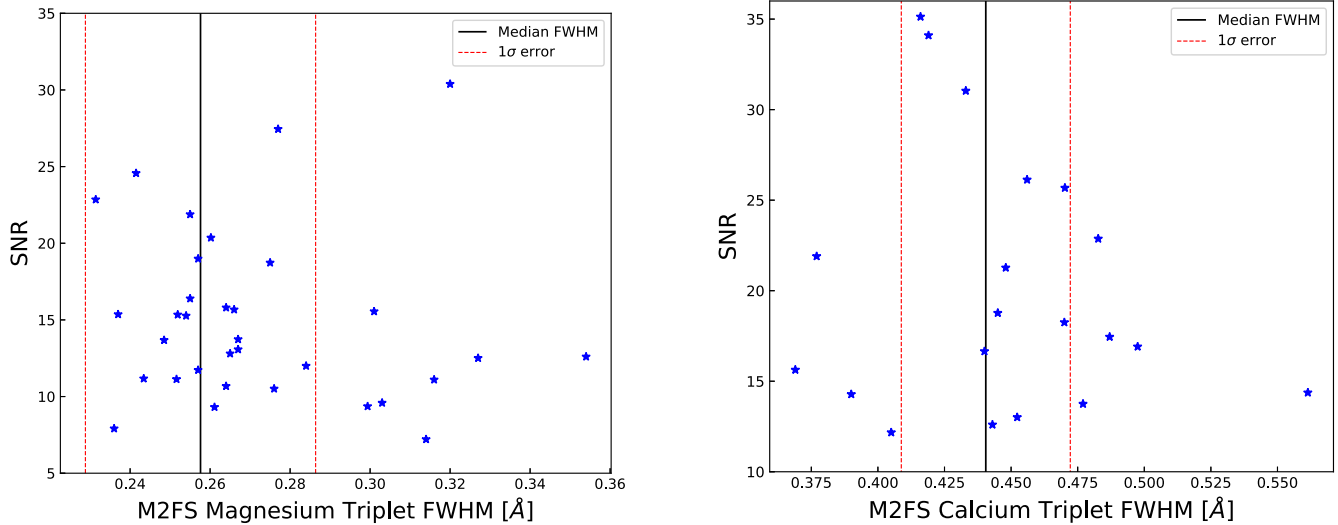


Figure A1. Line-spread function determination for Mg and Ca M2FS data. We restricted our line-spread function determination for the stars in our field with $S/N \geq 20$.

velocity dispersion measurements of 48 clusters. This more than doubles the sample of reliable velocity dispersion measurements, and represents measurements of nearly half of all luminous GCs around Cen A.

To determine radii for these clusters, we updated the BP-RP Gaia excess factor and half-light radii relation from Voggel et al. (2020) using Gaia EDR3 (Riello et al. 2021). Gaia EDR3 is more complete than Gaia DR2 used in Voggel et al. (2020) and the BP-RP excess factor has been recalculated. This revised relation (Equation (2)) can be used to estimate half-mass radii for extragalactic GCs with sizes $< 1''$ to an accuracy of 14%.

We combine size measurements with the derived velocity dispersions to determine virial masses and V -band mass-to-light ratio for 57 luminous GCs. We find a bimodal distribution of M/L_V with a second population of elevated mass-to-light ratios ($M/L_V > 2.3$). Using a two component Gaussian mixture model we find that 35% (20/57) of our luminous GC have inflated M/L_V .

Our preferred explanation for the elevated M/L_V in these clusters is the presence of high mass fraction central black holes in the clusters. We create JAM dynamical models based on the integrated velocity dispersion to derive the central black hole mass needed to produce the elevated mass-to-light ratio. We find that black hole masses comprising 4%–18% of the luminous GC mass can explain the elevated mass-to-light ratios in these clusters. The maximum inferred BH mass is $8.61^{+10.3}_{-0.12} \times 10^5 M_\odot$ for the cluster *VHH81-01*. The possible presence of high mass fraction black holes supports the idea that some or even all of the 20 luminous GCs with elevated M/L_V are the remnant nuclear star clusters of stripped galaxies. Future high spatial resolution kinematic observations will be able to verify directly if these clusters contain high mass fraction black holes.

Work by A.D. and A.C.S. has been supported by NSF AST-1813609. AKH and DJS acknowledge support from NSF grants AST-1821967 and 1813708. NC acknowledges support by NSF grant AST-1812461. JS acknowledges support from NSF grant AST-1812856 and the Packard Foundation. We

thank Christian I. Johnson for his recipe book for reducing M2FS data. We also thank Paul Martini for providing the MIKE spectroscopic data for 14 luminous GCs from his 2004 paper, and Pauline Barmby for globular cluster structural properties from McLaughlin et al. (2008).

This paper made use of the the MGE fitting method and software by Cappellari (2002) and JAM modeling method of Cappellari (2008), as well as the astropy package (Astropy Collaboration et al. 2013).











Facility: Magellan:Clay (LDSS2 imaging spectrograph).

Appendix HST V-band Magnitudes

Figure A1 shows the derived FWHM of the stars used to measure the intrinsic LSF for the M2FS Magnesium Triplet and M2FS Calcium Triplet. The complete list of 321 luminous GCs candidates with their measured radial velocities and luminosity-weighted metallicities can be found in Table 2. The list of the 57 luminous GCs with measured velocity dispersions is presented in Table 3. Finally, the list of updated half-mass radii and mass-to-light ratios for 15 literature CenA’s GCs are shown in Table 4. We found five objects (*T17-1498*, *T17-1511*, *KV-280*, *KV19-289*, *T17-1614*) where the magnitudes had large differences between their (very bright) NOAO DR2 values and (fainter) Gaia magnitudes (i.e., $|g - G| > 2$). PISCeS imaging cutouts for these objects show they are in crowded or star-forming regions that affect the ability to obtain reliable aperture photometry as is used for the NOAO catalog. Fortunately, all five objects had available HST F555W imaging—we obtained V -band magnitudes from the HST Legacy Archive SExtractor catalogs F555W SExtractor imaging photometry. Because F555W are Vega-based magnitudes, we assume they are equal to V -band magnitudes. ($V - F555W = 0.02$ – 0.4 based on old stellar populations from Marigo et al. 2017) models of 0.02 – 0.04 for old stellar populations). Additionally, three luminous GCs have $g - r$ colors not consistent with the rest of our luminous GCs. *KV19-273* and *KV19-295* have very red colors, $g - r > 1.1$, and *T17-1648* a very blue color of $g - r \sim 0.1$ mag. PISCeS imaging cutouts for these objects show that two are in crowded regions and one is close to a

bright star. Only *KV19-273* has available HST F555W imaging, and we were able to obtain *V*-band magnitude as described above. For *KV19-295* and *T17-1648* their bad *g* – *r* color affects our ability to estimate *V*-band magnitudes, and their *V*-band magnitudes may be wrong. Two more luminous GCs, *Fluffy* and *VHH81-5*, and a nuclear star cluster, *ESO269-06*, were not present in the Gaia EDR3 source catalog, and we estimated their sizes from fits to HST imaging data (see Section 4.1). To be consistent, we estimated their *V*-band magnitude from the same data assuming $V-F606W \sim 0.25$ based on expected colors for metal-poor old stellar populations using Padova Single Stellar Population (SSP) models (Marigo et al. 2017). Finally, we use the *V*-band magnitude of the nuclear star cluster of *KK197-NSC* from Georgiev et al. (2009). We correct for foreground extinction for these 10 sources using the same recipe as that for the NOAO DR2 photometry (see Section 2.1).

ORCID iDs

Antoine Dumont  <https://orcid.org/0000-0003-0234-3376>
 Anil C. Seth  <https://orcid.org/0000-0003-0248-5470>
 Jay Strader  <https://orcid.org/0000-0002-1468-9668>
 Karina Voggel  <https://orcid.org/0000-0001-6215-0950>
 David J. Sand  <https://orcid.org/0000-0003-4102-380X>
 Allison K. Hughes  <https://orcid.org/0000-0002-1718-0402>
 Nelson Caldwell  <https://orcid.org/0000-0003-2352-3202>
 Denija Crnojević  <https://orcid.org/0000-0002-1763-4128>
 John I. Bailey, III  <https://orcid.org/0000-0002-4272-263X>
 Duncan A. Forbes  <https://orcid.org/0000-0001-5590-5518>

References

- Afanasiev, A. V., Chilingarian, I. V., Mieske, S., et al. 2018, *MNRAS*, **477**, 4856
- Ahn, C. P., Seth, A. C., Cappellari, M., et al. 2018, *ApJ*, **858**, 102
- Ahn, C. P., Seth, A. C., den Brok, M., et al. 2017, *ApJ*, **839**, 72
- Alfaro-Cuello, M., Kacharov, N., Neumayer, N., et al. 2019, *ApJ*, **886**, 57
- Astropy Collaboration, Robitaille, T. P., Tollerud, E. J., et al. 2013, *A&A*, **558**, A33
- Beasley, M. A., Bridges, T., Peng, E., et al. 2008, *MNRAS*, **386**, 1443
- Bernstein, R., Shectman, S. A., Gunnels, S. A., Mochnacki, S., & Athey, A. E. 2003, *Proc SPIE*, **4841**, 1694
- Bruzual, G., Charlot, S., Lópezlira, R. G., et al. 2013, in IAU Symp. 295, The Intriguing Life of Massive Galaxies, ed. D. Thomas, A. Pasquali, & I. Ferreras (Cambridge: Cambridge Univ. Press), **282**
- Cappellari, M. 2002, *MNRAS*, **333**, 400
- Cappellari, M. 2008, *MNRAS*, **390**, 71
- Cappellari, M. 2017, *MNRAS*, **466**, 798
- Crnojević, D., Sand, D. J., Bennet, P., et al. 2019, *ApJ*, **872**, 80
- Crnojević, D., Sand, D. J., Caldwell, N., et al. 2014, *ApJL*, **795**, L35
- Crnojević, D., Sand, D. J., Spekkens, K., et al. 2016, *ApJ*, **823**, 19
- Dabringhausen, J., Kroupa, P., & Baumgardt, H. 2009, *MNRAS*, **394**, 1529
- Di Carlo, U. N., Mapelli, M., Pasquato, M., et al. 2021, *MNRAS*, **507**, 5132
- Fabricius, C., Luri, X., Arenou, F., et al. 2021, *A&A*, **649**, A5
- Fahron, K., Müller, O., Rejkuba, M., et al. 2020, *A&A*, **634**, A53
- Forbes, D. A. 2020, *MNRAS*, **493**, 847
- Forbes, D. A., & Kroupa, P. 2011, *PASA*, **28**, 77
- Forbes, D. A., Norris, M. A., Strader, J., et al. 2014, *MNRAS*, **444**, 2993
- Georgiev, I. Y., Puzia, T. H., Hilker, M., & Goudfrooij, P. 2009, *MNRAS*, **392**, 879
- Graham, A. W. 2016, in IAU Symp. 312, Star Clusters and Black Holes in Galaxies across Cosmic Time, ed. Y. Meiron et al. (Cambridge: Cambridge Univ. Press), **269**
- Graham, A. W. 2020, *MNRAS*, **492**, 3263
- Greene, J. E., Strader, J., & Ho, L. C. 2020, *ARA&A*, **58**, 257
- Hanuschik, R. W. 2003, *A&A*, **407**, 1157
- Harris, G. L. H., Gómez, M., Harris, W. E., et al. 2012, *AJ*, **143**, 84
- Harris, G. L. H., Harris, W. E., & Geisler, D. 2004, *AJ*, **128**, 723
- Harris, G. L. H., Rejkuba, M., & Harris, W. E. 2010, *PASA*, **27**, 457
- Harris, W. E., Harris, G. L. H., Holland, S. T., & McLaughlin, D. E. 2002, *AJ*, **124**, 1435
- Hénault-Brunet, V., Gieles, M., Strader, J., et al. 2020, *MNRAS*, **491**, 113
- Hesser, J. E., Harris, H. C., & Harris, G. L. H. 1986, *ApJL*, **303**, L51
- Hughes, A. K., Sand, D. J., Seth, A., et al. 2021, *ApJ*, **914**, 16
- Husser, T. O., Wende-von Berg, S., Dreizler, S., et al. 2013, *A&A*, **553**, A6
- Inayoshi, K., Visbal, E., & Haiman, Z. 2020, *ARA&A*, **58**, 27
- Jester, S., Schneider, D. P., Richards, G. T., et al. 2005, *AJ*, **130**, 873
- Jefábková, T., Kroupa, P., Dabringhausen, J., Hilker, M., & Bekki, K. 2017, *A&A*, **608**, A53
- Johnson, C. I., & Pilachowski, C. A. 2010, *ApJ*, **722**, 1373
- Karachentseva, V. E., & Karachentsev, I. D. 1998, *A&AS*, **127**, 409
- Kelson, D. D. 2003, *PASP*, **115**, 688
- Kelson, D. D., Illingworth, G. D., van Dokkum, P. G., & Franx, M. 2000, *ApJ*, **531**, 159
- King, I. 1962, *AJ*, **67**, 471
- King, I. R. 1966, *AJ*, **71**, 64
- Krajnović, D., Cappellari, M., McDermid, R. M., et al. 2018, *MNRAS*, **477**, 3030
- Kroupa, P., Subr, L., Jerabkova, T., & Wang, L. 2020, *MNRAS*, **498**, 5652
- Kruijssen, J. M. D. 2008, *A&A*, **486**, L21
- Kruijssen, J. M. D., Pfeffer, J. L., Reina-Campos, M., Crain, R. A., & Bastian, N. 2019, *MNRAS*, **486**, 3180
- Larsen, S. S. 1999, *A&AS*, **139**, 393
- Lauberts, A. 1982, ESO/Uppsala survey of the ESO(B) atlas (Garching: ESO)
- Liu, C., Peng, E. W., Toloba, E., et al. 2015, *ApJL*, **812**, L2
- Mahani, H., Zonoozi, A. H., Haghi, H., et al. 2021, *MNRAS*, **502**, 5185
- Marigo, P., Girardi, L., Bressan, A., et al. 2017, *ApJ*, **835**, 77
- Martini, P., & Ho, L. C. 2004, *ApJ*, **610**, 233
- Mateo, M., Bailey, J. I., Crane, J., et al. 2012, *Proc. SPIE*, **8446**, 84464Y
- Mayes, R. J., Drinkwater, M. J., Pfeffer, J., et al. 2021, *MNRAS*, **501**, 1852
- McLaughlin, D. E., Barmby, P., Harris, W. E., Forbes, D. A., & Harris, G. L. H. 2008, *MNRAS*, **384**, 563
- Mieske, S., Frank, M. J., Baumgardt, H., et al. 2013, *A&A*, **558**, A14
- Mieske, S., & Kroupa, P. 2008, *ApJ*, **677**, 276
- Miller, B. P., Gallo, E., Greene, J. E., et al. 2015, *ApJ*, **799**, 98
- Neumayer, N., Seth, A., & Böker, T. 2020, *A&ARv*, **28**, 4
- Nguyen, D. D., Seth, A. C., Neumayer, N., et al. 2018, *ApJ*, **858**, 118
- Nguyen, D. D., Seth, A. C., Neumayer, N., et al. 2019, *ApJ*, **872**, 104
- Nidever, D. L. & Astro Data Lab team 2020, NSCG: NOIRLab Source Catalog Generator, Astrophysics Source Code Library, ascl:2012.002
- Norris, M. A., Escudero, C. G., Faifer, F. R., et al. 2015, *MNRAS*, **451**, 3615
- Norris, M. A., van de Ven, G., Kannappan, S. J., Schinnerer, E., & Leaman, R. 2019, *MNRAS*, **488**, 5400
- Palmer, B. A., & Engleman, R. J. 1983, Atlas of the thorium spectrum, LA-9615, Los Alamos National Lab, <https://www.osti.gov/biblio/6348879>
- Pechetti, R., Seth, A., Cappellari, M., et al. 2017, *ApJ*, **850**, 15
- Pechetti, R., Seth, A., Kamann, S., et al. 2022, *ApJ*, **924**, 48
- Peng, E. W., Ford, H. C., & Freeman, K. C. 2004, *ApJS*, **150**, 367
- Pfeffer, J., & Baumgardt, H. 2013, *MNRAS*, **433**, 1997
- Pfeffer, J., Griffen, B. F., Baumgardt, H., & Hilker, M. 2014, *MNRAS*, **444**, 3670
- Pfeffer, J., Hilker, M., Baumgardt, H., & Griffen, B. F. 2016, *MNRAS*, **458**, 2492
- Pfeffer, J., Lardo, C., Bastian, N., Saracino, S., & Kamann, S. 2021, *MNRAS*, **500**, 2514
- Portegies Zwart, S. F., Baumgardt, H., Hut, P., Makino, J., & McMillan, S. L. W. 2004, *Natur*, **428**, 724
- Reines, A. E., & Volonteri, M. 2015, *ApJ*, **813**, 82
- Rejkuba, M. 2001, *A&A*, **369**, 812
- Rejkuba, M., Dubath, P., Minniti, D., & Meylan, G. 2007, *A&A*, **469**, 147
- Ricarte, A., Tremmel, M., Natarajan, P., Zimmer, C., & Quinn, T. 2021, *MNRAS*, **503**, 6098
- Riello, M., De Angeli, F., Evans, D. W., et al. 2021, *A&A*, **649**, A3
- Schlafly, E. F., & Finkbeiner, D. P. 2011, *ApJ*, **737**, 103
- Scott, N., Graham, A. W., & Schombert, J. 2013, *ApJ*, **768**, 76
- Seth, A. C. 2010, *ApJ*, **725**, 670
- Seth, A. C., Dalcanton, J. J., Hodge, P. W., & Debattista, V. P. 2006, *AJ*, **132**, 2539
- Seth, A. C., van den Bosch, R., Mieske, S., et al. 2014, *Natur*, **513**, 398
- Siegel, M. H., Dotter, A., Majewski, S. R., et al. 2007, *ApJL*, **667**, L57
- Spengler, C., Côté, P., Roediger, J., et al. 2017, *ApJ*, **849**, 55
- Strader, J., Caldwell, N., & Seth, A. C. 2011, *AJ*, **142**, 8
- Strader, J., Smith, G. H., Larsen, S., Brodie, J. P., & Huchra, J. P. 2009, *AJ*, **138**, 547
- Taylor, M. A., Puzia, T. H., Gomez, M., & Woodley, K. A. 2015, *ApJ*, **805**, 65
- Taylor, M. A., Puzia, T. H., Harris, G. L., et al. 2010, *ApJ*, **712**, 1191

- Taylor, M. A., Puzia, T. H., Muñoz, R. P., et al. 2017, [MNRAS](#), **469**, 3444
- Tremou, E., Strader, J., Chomiuk, L., et al. 2018, [ApJ](#), **862**, 16
- van den Bergh, S., Hesser, J. E., & Harris, G. L. H. 1981, [AJ](#), **86**, 24
- Villanova, S., Geisler, D., Gratton, R. G., & Cassisi, S. 2014, [ApJ](#), **791**, 107
- Voggel, K. T., Seth, A. C., Baumgardt, H., et al. 2019, [ApJ](#), **871**, 159
- Voggel, K. T., Seth, A. C., Neumayer, N., et al. 2018, [ApJ](#), **858**, 20
- Voggel, K. T., Seth, A. C., Sand, D. J., et al. 2020, [ApJ](#), **899**, 140
- Woodley, K. A., Gómez, M., Harris, W. E., Geisler, D., & Harris, G. L. H. 2010, [AJ](#), **139**, 1871
- Woodley, K. A., Harris, W. E., Beasley, M. A., et al. 2007, [AJ](#), **134**, 494
- Woodley, K. A., Harris, W. E., & Harris, G. L. H. 2005, [AJ](#), **129**, 2654
- Zocchi, A., Gieles, M., & Hénault-Brunet, V. 2019, [MNRAS](#), **482**, 4713